The initial conditions of observed star clusters – I. Method description and validation

J. T. Pijloo,[1,2]⋆ S. F. Portegies Zwart,[2] P. E. R. Alexander,[3] M. Gieles,[4] S. S. Larsen,[1] P. J. Groot[1] and B. Devecchi[5]

[1]*Department of Astrophysics/IMAPP, Radboud University, PO Box 9010, NL-6500 GL Nijmegen, the Netherlands*
[2]*Leiden Observatory, Leiden University, PO Box 9513, NL-2300 RA Leiden, the Netherlands*
[3]*Institute of Astronomy, University of Cambridge, Madingley Road, Cambridge CB3 0HA, UK*
[4]*Department of Physics, University of Surrey, Guildford GU2 7XH, UK*
[5]*TNO Defence, Security and Safety, The Hague, The Netherlands*

ABSTRACT

We have coupled a fast, parametrized star cluster evolution code to a Markov Chain Monte Carlo code to determine the distribution of probable initial conditions of observed star clusters, that may serve as a starting point for future *N*-body calculations. In this paper, we validate our method by applying it to a set of star clusters which have been studied in detail numerically with *N*-body simulations and Monte Carlo methods: the Galactic globular clusters M4, 47 Tucanae, NGC 6397, M22, ω Centauri, Palomar 14 and Palomar 4, the Galactic open cluster M67, and the M31 globular cluster G1. For each cluster, we derive a distribution of initial conditions that, after evolution up to the cluster's current age, evolves to the currently observed conditions. We find that there is a connection between the morphology of the distribution of initial conditions and the dynamical age of a cluster and that a degeneracy in the initial half-mass radius towards small radii is present for clusters that have undergone a core collapse during their evolution. We find that the results of our method are in agreement with *N*-body and Monte Carlo studies for the majority of clusters. We conclude that our method is able to find reliable posteriors for the determined initial mass and half-mass radius for observed star clusters, and thus forms an suitable starting point for modelling an observed cluster's evolution.

Key words: methods: numerical – galaxies: star clusters: general.

1 INTRODUCTION

What were the initial conditions of the star clusters we observe today? Answering this question not only requires accurate observations of the current conditions, but also proper modelling of star cluster evolution over a large amount of time (for a globular cluster typically 12 Gyr), taking into account a number of physical processes, such as two-body relaxation, three- and four-body interactions, the stellar evolution of single and binary stars and the effects of a galactic tidal field (Ambartsumian 1938; Chandrasekhar 1942; King 1958; Hénon 1960; Lee & Ostriker 1987; Hut et al. 1992). The required complexity of the simulation depends on the type of cluster one wishes to model and the physics question to be answered. In the Milky Way Galaxy, we know 157 globular clusters (Harris 2010), and about 2200 Galactic star clusters in the disc. Of the

latter, ∼2170 are relatively low-mass ($<10^4$ M$_\odot$) systems that we traditionally classify as open clusters (Dias et al. 2002 version 3.3 – 2013 January 10), while ∼30 have masses and luminosities comparable to the type of clusters that are typically found in studies of external galaxies, classified as young massive ($>10^4$M$_\odot$) clusters (Portegies Zwart, McMillan & Gieles 2010). The obvious differences between these three cluster types lie in the age, the number of stars, the (half-mass) density and the amount of gas currently present in the cluster. Each factor complicates the simulation of the cluster evolution, if its value is high. However, at the basic level, each of these star clusters is subject to the same physical processes (Larsen 2002) and will eventually meet the same fate of complete dissolution (Aarseth 1973; Baumgardt 2006).

1.1 Star cluster physics

Star clusters form in the collapse of giant molecular clouds (see e.g. Alves, Lada & Lada 2001; Molinari et al. 2014). After the

⋆ E-mail: t.pijloo@astro.ru.nl

complex phases of cluster formation and early evolution with residual gas expulsion, cluster expansion and re-virialization (see e.g. Baumgardt & Kroupa 2007; Pelupessy & Portegies Zwart 2012; Banerjee & Kroupa 2013; Longmore et al. 2014), the star cluster is often assumed to evolve as a roughly spherically symmetric gas-less system under the influence of the following physical processes:

(i) the dynamics of the stars on both the large scale (two-body relaxation) and on the small scale (three- and four-body interactions, binary formation and evolution; Ambartsumian 1938; Chandrasekhar 1942; King 1958);

(ii) the stellar evolution of single stars and binaries (Hut et al. 1992);

(iii) the interaction with the tidal field of the galaxy it resides in (Hénon 1960; Lee & Ostriker 1987).

Two-body relaxation tends to drive the cluster to the unreachable state of equipartition, where the kinetic energy of the stars in the cluster is equalized, see e.g. Khalisi, Amaro-Seoane & Spurzem (2007) and the references therein. This has two major effects: (1) mass segregation (MS): the most massive stars will sink to the cluster centre, whereas the lower mass stars populate the halo; (2) core-collapse: due to the decrease of kinetic energy in the core, gravitational collapse is no longer supported. Hence, the core will shrink until high enough core densities are reached to produce a new source of kinetic energy: binaries (Aarseth 1973). The binaries will halt the process of core-collapse and start the core expansion by interacting with less massive stars, in which the former become more tightly bound ('hard') and the latter escape into the halo of the cluster (Aarseth 1973). The half-mass radius will increase driven by stellar evolution and hard binaries (Gieles et al. 2010). Since the low-mass components transferred to the halo have higher kinetic energy, this process will also cause the preferential loss of low-mass stars. The escape of stars over the tidal radius leads to a contraction of the cluster, i.e. the decrease of the half-mass radius, at a (roughly) constant density (Hénon 1961, 2011; Gieles, Heggie & Zhao 2011). If, on the other hand, the cluster has a significant amount of primordial binaries ($\gtrsim 10$ per cent), either the core-collapse would be less deep in the sense that the core radius would not decrease as much as it would without the presence of primordial binaries, or there would be no core-collapse at all, see e.g. Baumgardt et al. (2003a).

1.2 Simulation techniques

In computational astronomy great progress has been made to develop dedicated codes to study the evolution of star clusters. These dedicated codes can roughly be divided in three groups (Alexander & Gieles 2012). The first group of methods are the *N*-body simulations. Direct *N*-body simulations (e.g. Aarseth 1973; Makino 1996; Spurzem 1999) have the smallest number of simplifying assumptions. The time complexity of these simulations scales with N^2, where *N* is the number of stars in the simulation, and solutions up to arbitrary precision can be obtained, see Portegies Zwart & Boekholt (2014) and Boekholt & Portegies Zwart (2015). The N^2 time complexity makes these simulations computationally expensive. Globular clusters contain tens of thousands to several millions of stars at the present day, and theoretical motivations point out that they must have had an even greater initial number of stars (Aarseth 1973). Because of this large initial number of stars a direct *N*-body simulation of the evolution of a million body globular cluster over its entire lifetime is yet to be performed. Direct *N*-body simulations with fewer stars that are scaled up afterwards to match the observed clusters, have been made successfully, and also the direct *N*-body integration of small globular clusters, or of open clusters, has been done with success, see e.g. Baumgardt et al. (2003b), Zonoozi et al. (2011, 2014) and Hurley et al. (2005) for *N*-body simulations of the evolution of G1, Palomar 14, Palomar 4 and M67, respectively. For the less accurate, but more efficient, tree-codes the computation time-scales with $N\log(N)$; see Bédorf & Portegies Zwart (2012) for a review of the history of the collisional direct and collision-less tree-code *N*-body methods.

Other methods, such as Monte Carlo methods (Metropolis & Ulam 1949; Freitag & Benz 2001; Giersz 2006; Giersz, Heggie & Hurley 2008) and Fokker Planck models (Kolmogoroff 1931; Cohn 1979), scale with *N* and make some simplifying assumptions such that the computational cost decreases, but at the price of the decrease of the accuracy. With this second group of methods, the computation of the evolution of globular clusters with initially more than 10^6 stars has become possible, but can still take a substantial amount of time and computer power. Therefore, the choice of initial conditions is very important and a lot of effort is usually put into choosing a plausible set of initial conditions that will evolve to a cluster with characteristics similar to the observed cluster of interest. See e.g. Giersz & Heggie (2009) where a number of small scale runs, i.e. simulations for clusters with a lower initial number of stars, are performed to this end.

The third group of methods are the gaseous models (Larson 1970) and the semi-analytical methods, where the computation time is approximately *N*-independent. The semi-analytical methods make use of parametric equations for the evolution of the cluster variables, such as the number of stars, *N*, and the half-mass radius, $r_{\rm hm}$, which are then solved with a numerical integrator. These methods are therefore faster again. One such code is the recently developed Evolve Me A Cluster of StarS (EMACSS) code, which is based on the flow of energy in a cluster and allows one to compute the evolution of a globular cluster over 12 Gyr in a fraction of a second (Alexander & Gieles 2012; Alexander et al. 2014; Gieles et al. 2014). This code has been tested against *N*-body simulations and has proven to be an extremely powerful tool in understanding cluster evolution and exploring large regions in initial parameter space.

1.3 Goal of this work

We aim to determine the most probable sets of initial conditions in total cluster mass, *M*, and half-mass radius, $r_{\rm hm}$, for any observed star cluster and explore possible degeneracies. Finding the initial conditions of individual star clusters has been done before, see e.g. Giersz & Heggie (2003), Baumgardt et al. (2003b), Hurley et al. (2005), Heggie & Giersz (2008), Giersz & Heggie (2009), Giersz & Heggie (2011), Zonoozi et al. (2011), Heggie & Giersz (2014) and Zonoozi et al. (2014). These studies used elaborate simulation techniques to model cluster evolution and found suitable initial conditions that, after evolving up to the cluster's age, resembled a number of observables of their star cluster of interest. However, due to the versatility of their methods, these studies were only able to investigate up to several tens of sets of initial conditions iteratively. They could not investigate the uniqueness of their sets of initial conditions or explore whether there are multiple, significantly different, sets of initial conditions that evolve to the current observables, i.e. whether there are degeneracies. In this study, we aim to address this latter point as well. We accomplish this by coupling the fast, parametrized star cluster evolution code EMACSS (Alexander et al. 2014) to the Markov Chain Monte Carlo (MCMC) code EMCEE (Foreman-Mackey et al. 2013).

In this paper, we describe and demonstrate our method. We validate it by applying it to nine star clusters that have been studied to great extent with either *N*-body simulations or Monte Carlo methods and by comparing our results to the results of those methods. The paper is organized as follows: in Section 2, we explain our method and we summarize the functionality of the underlying star cluster evolution code. In Section 4.4, we describe our validation strategy and set out the relevant parts of the extensive work that has been done on the validation clusters by other authors. In Section 4, we show our results and we discuss them in detail. Section 5 summarizes the paper and discusses future work.

2 METHOD

2.1 The parametrized star cluster evolution code

We evolve the star clusters using the parametrized star cluster evolution code EMACSS (Alexander & Gieles 2012; Gieles et al. 2014; Alexander et al. 2014). EMACSS includes a prescription for MS, the evolution of the mean stellar mass, $\tilde{m} = M/N$, as the result of stellar evolution, the resulting expansion of the cluster and the escape of stars over the tidal radius, r_t. After a phase of 'unbalanced' evolution, in which the evolution and escape of stars are the dominant drivers of the evolution, a phase of 'balanced' evolution starts (Alexander et al. 2014). Here, it is assumed that the core produces the correct amount of energy to sustain the two-body relaxation process. Balanced evolution is assumed to start after a fixed number of (half-mass) relaxation times.

A cluster is evolved on a circular orbit, with constant orbital velocity, v, at a constant galactocentric radius, R_{GC}, about the galactic centre. EMACSS assumes a logarithmic potential, ϕ, for the galaxy that imposes a static tidal field on the cluster (Alexander et al. 2014; Gieles et al. 2014),

$$\phi = v^2 \ln(R_{GC}) \tag{1}$$

$$r_J^3 = \frac{GMR_{GC}^2}{2v^2}, \tag{2}$$

in which r_J is the Jacobi radius and G is the gravitational constant. Note that $r_J = r_t$ for the type of potential used here.

The code uses a Kroupa initial mass function (IMF; Kroupa 2001) with a lower mass limit of $0.1\,M_\odot$ and an optional upper mass limit m_{up}. It was tested against *N*-body simulations for $m_{up} = 15\,M_\odot$ or $100\,M_\odot$ with an initial mean mass of $0.64\,M_\odot$ in both cases (Alexander et al. 2014). In each of our simulations, we use the upper mass limit of $100\,M_\odot$ and an initial mean mass of $0.64\,M_\odot$. EMACSS furthermore offers an indication of core-collapse based on an 'average' cluster, which is adequate to determine the state of a cluster substantially before or after core collapse, although is unreliable at times within a factor $\sim$2 of the predicated collapse itself. The code does not explicitly include a prescription for stellar interactions and binary formation, nor does it account for the effects of a primordial binary population. This most recent version of EMACSS also allows one to take into account the effects of dynamical friction. We have not included this feature in the simulations in this paper, because the studies we compare our results to have not included this effect either. We will explore the effects of dynamical friction in forthcoming work. The details of EMACSS are described in references mentioned above.

The most recent version of EMACSS (Alexander et al. 2014) is available on GitHub[1] and in the Astrophysical Multipurpose Software Environment (AMUSE; Portegies Zwart et al. 2009).[2]

2.2 EMACSS-MCMC method

We define a set of initial conditions of a star cluster as the cluster's initial mass and initial half-mass radius, i.e. $(M_i, r_{hm, i})$. We constrain the initial conditions for an observed star cluster from the observed current mass, M_{obs}, half-mass radius, $r_{hm, obs}$, age, τ_{obs}, galactocentric radius, $R_{GC, obs}$ and orbital velocity, v_{obs}. For each observed cluster, we simulate *n* clusters with different initial total masses and half-mass radii, M_i and $r_{hm, i}$ respectively, from $t = 0$ Gyr to $t = \tau_{obs}$. These clusters all start out with the same initial galactocentric radius and initial orbital velocity, equal to the currently observed values,[3] since both these parameters do not change throughout the evolution with EMACSS without dynamical friction. After evolving the clusters, we compare their final conditions in mass and half-mass radius, i.e. M_f and $r_{hm, f}$ respectively, to the observed present-day values and assign a (posterior) probability to each initial condition. Note that the zero age of the cluster, i.e. $t = 0$ Gyr, is defined in EMACSS as the time when both the residual gas of the giant molecular gas cloud, from which the star cluster formed, has escaped the cluster and the cluster has reached virial equilibrium.

For choosing the initial conditions in mass and half-mass radius, we could have used a grid of *n* mass and half-mass radius pairs, e.g. evenly spaced in both half-mass radius and (the logarithm of) mass. However, if one wants to determine the initial conditions in more than two dimensions, which we do in our 5D simulations (see Section 3.1.2), the grid approach is no longer feasible and one needs to sample the initial conditions with a method that efficiently probes and properly covers a multidimensional parameter space. We therefore use the affine-invariant ensemble sampler for MCMC as coded up in the EMCEE code (Foreman-Mackey et al. 2013) based on Goodman & Weare (2010).

MCMC is a procedure to generate a random walk in parameter space to obtain an approximation to the *unknown* posterior density distribution function (PDF; Metropolis et al. 1953; Hastings 1970; Foreman-Mackey et al. 2013). Sampling the PDF starts by initializing the *walkers* across parameter space according to some *prior* distribution. The walkers then sample parameter space according to the specific MCMC algorithm one employs, and eventually converge towards those regions of parameter space with high posterior probability. Since in most cases one has no a priori knowledge what the PDF looks like, the simplest and most uninformative prior – a uniform distribution in each parameter/dimension – can be used. The walkers *burn-in* to probable regions of parameter space that can then be used as a starting point of the subsequent (chain iteration) phase (Foreman-Mackey et al. 2013).[4]

---

[1] https://github.com/emacss/emacss
[2] http://amusecode.org/
[3] In this section, we describe the general use of the two-dimensional version of our method. However, since our aim is to validate our method, we choose the same values for the age, the galactocentric radius and the orbital velocity as the studies we compare to in our 2D simulations, but in our 5D simulations we will marginalize over these three parameters in the five-dimensional version of our method, see Section 3.1.2.
[4] The *burn-in* is defined as the first part of the Markov chain where the walkers reach a certain level of posterior probability, but is otherwise the same as the subsequent *chain iteration phase*. Since the first part of the Markov chain usually contains lower probabilities, it is common prac-
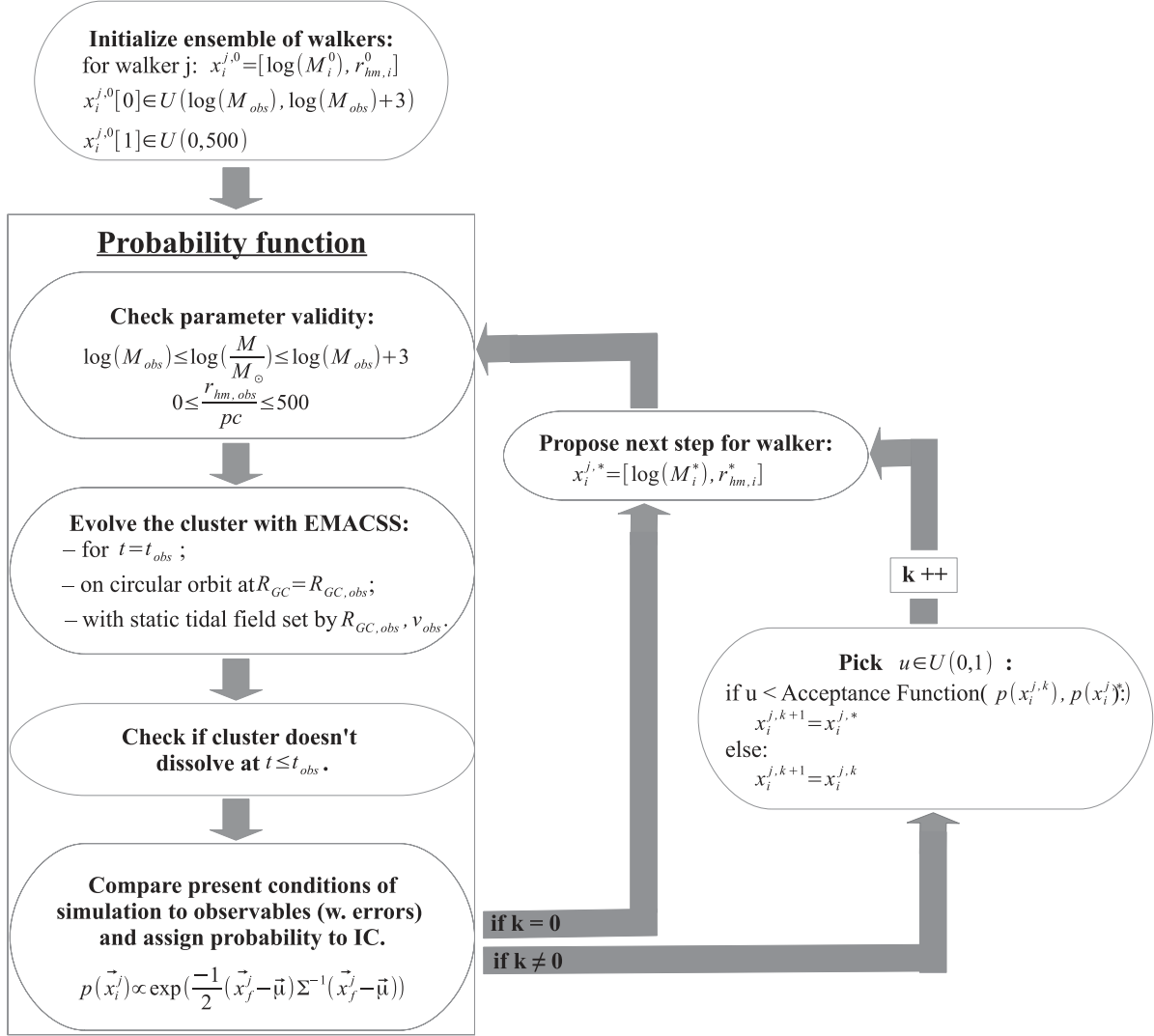
Figure 1. The schematic representation of our method. One round through this scheme represents one iteration, both the burn-in and subsequent chain iteration phase.

Fig. 1 presents the method we employ. One round through the scheme represents one iteration. For each of the observed clusters, we sample a two-dimensional parameter space, in $\log(M)$ and r_{hm}. We use $\log(M)$ instead of M, because we experienced that the MCMC method is more efficient when it covers the large range of several orders of magnitude in mass in logarithmic space than in linear space. We use an ensemble of n_w walkers, a burn-in phase of n_b iterations and n_c subsequent (chain) iterations such that evolve a total of $n = n_w(1 + n_b + n_c)$ clusters. A walker j at iteration k is defined as $\boldsymbol{x}_i^{j,k} = [\log(M_i^{j,k}), r_{hm,i}^{j,k}]$; the subscript i denotes that it concerns an initial condition. We use the following boundary conditions for the parameters:

$$\log(M_{obs}) \leq \log(\frac{M}{M_\odot}) \leq \log(M_{obs}) + 3,$$

$$0 < \frac{r_{hm}}{pc} < 500, \tag{3}$$

tice to remove the data of the burn-in phase from the results such that further analysis is not biased by the low probabilities of the burn-in. See e.g. Putze et al. (2009) for a nice explanation of the burn-in phase.

in which the lower mass boundary comes from the fact that the initial cluster must have been at least as massive as it is today. The other boundaries were found to be reasonable values to not exclude any possibly interesting regions in mass and half-mass radius and to get a good balance between proper coverage and quick convergence. For the initialization, we have experimented with several different prior distributions, see Section 4.1. When the walkers are initialized, they are evaluated in the probability function, see Fig. 1. The probability function determines how suitable the sets of initial conditions are for the observed cluster of interest by assigning a posterior probability, p, to each initial condition; p takes value in the range 0–1 where 0 denotes the lowest probability and 1 denotes the highest probability. This is done as follows.

(i) *Initial condition check*: for a walker j at iteration k it checks whether its mass and half-mass radius, stored in $\boldsymbol{x}_i^{j,k}[0]$ and $\boldsymbol{x}_i^{j,k}[1]$, respectively, are within the ranges of equation (3). If a certain initial condition is in the requested range, it proceeds to step (ii). If this is not the case, steps (ii)–(iv) will be skipped and this initial condition is assigned a posterior probability $p = 0$.

(ii) *Evolution*: a cluster with this walker's initial mass and half-mass radius will be evolved with EMACSS, at a constant galactocentric radius $R_{GC} = R_{GC, obs}$ and velocity $v = v_{obs}$ from $t = 0$ Gyr until the observed cluster's age $t = \tau_{obs}$ is reached. It proceeds to step (iii).

(iii) *Dissolution check*: it checks whether the cluster dissolved before reaching $t = \tau_{obs}$. If for a certain set of initial conditions, the cluster dissolved before reaching the age $t = \tau_{obs}$, step (iv) will be skipped and this initial condition is assigned a posterior probability $p = 0$. If the cluster stayed bound until $t = \tau_{obs}$, it proceeds to step (iv).

(iv) *Posterior probability calculation:* the final conditions of the cluster – for a walker j at iteration k contained in $\mathbf{x}_f^{j,k} = [\log(M_f^{j,k}), r_{hm,f}^{j,k}]$, where the subscript f denotes that it concerns a final condition – are compared to the observables and a posterior probability p is calculated according to

$$ln(p) = -\frac{1}{2}\left((\mathbf{x}_f^{j,k} - \boldsymbol{\mu})^T \Sigma^{-1} (\mathbf{x}_f^{j,k} - \boldsymbol{\mu}) \right), \tag{4}$$

in which $\boldsymbol{\mu} = [M_{obs}, r_{hm,obs}]$ are the present-day observed values and Σ^{-1} is the inverse of the covariance matrix which contains the errors in M_{obs} and $r_{hm, obs}$. We assume that the errors in mass and half-mass radius are not correlated such that the covariance matrix contains no non-zero off-diagonal elements:

$$\Sigma = \begin{pmatrix} |\log(M_{obs}) - \log(M_{obs} - \Delta M_{obs})| & 0 \\ 0 & \Delta r_{hm,obs} \end{pmatrix}. \tag{5}$$

We chose to use 10 per cent errors in both observables for all our clusters in the majority of our simulation; this choice is arbitrary and used in this paper as a proof of concept. In further applications of our method one can use the actual observational errors. In Section 4.3.4, we investigate what the effect of taking smaller (5 per cent) or larger (20 per cent) errors has on the results.

After an iteration k each walker will be proposed a new set of initial conditions for the next iteration $k + 1$. Whether the walker accepts or declines this proposed set is determined as follows: for a walker j a new set of initial conditions $\mathbf{x}_i^{j,*}$ will be proposed according to the *stretch move* algorithm. This is an algorithm in which one simultaneously evolves an ensemble of walkers, whereby the proposal distribution, from which the proposed initial condition is drawn, is based on the initial conditions for the other $n_w - 1$ walkers in the previous iteration (k), see Foreman-Mackey et al. (2013). This set of initial conditions is evaluated in the probability function, as explained above. After this set of initial conditions is assigned a posterior probability, p^*, p^* will be compared to the posterior probability of the previous iteration, p, and a probability q will be calculated for the acceptance of this proposed set of initial conditions, see equation 9 of Foreman-Mackey et al. (2013). The values of q are in the range 0–1 and will approach the value 1 if $p^* \gg p$ and the value 0 if $p^* \ll p$. Lastly, a random number u will be drawn from a uniform distribution between 0 and 1; if $q > u$ the walker j accepts the proposed set of initial conditions such that $\mathbf{x}_i^{j,k+1} = \mathbf{x}_i^{j,*}$, i.e. the walker 'walks' to this proposed set. If $q < u$, then $\mathbf{x}_i^{j,k+1} = \mathbf{x}_i^{j,k}$ and the walker 'stays' at its previous set of initial conditions. This procedure is repeated for all the iterations, both the burn-in iterations and the subsequent chain iterations. See Foreman-Mackey et al. (2013) for further details of the code EMCEE.

In Section 4.1, we first determine suitable values for the number of walkers, n_w, the number of burn-in iterations, n_b, and the number of subsequent chain iterations, n_c, while testing the performance of our method. Thereafter, we investigate the effect of different prior distributions on the determined distribution of probable initial conditions.

2.3 Correcting observations for MS

When one wishes to compare observed structural parameters to the simulated ones, it is of great importance that these parameters are obtained in the same way. Since it is observationally more practical to find the size of a cluster by determining the angular projected half-light radius in arcminutes (arcmin), whereas theoretically half-mass radii in parsec (pc) are more functional, some conversions are needed before a proper comparison between the simulations and the observations can be made.

The angular projected half-light radius, θ_{phl}, in arcmin from the observations can be converted to the projected half-light radius, r_{phl}, in pc once the distance from the Earth to the cluster, R_E, is known:

$$r_{phl} = \left(\frac{R_E}{pc} \right) \tan\left(\frac{\theta_{phl}}{arcmin} \times \frac{\pi}{10800} \right). \tag{6}$$

We calculate the *observational* half-mass radius, r_{hm}, for two extreme cases: with or without a correction for MS.

(i) Case 1: no correction for MS.
We assume that the cluster experienced no MS at $t = \tau_{obs}$ yet such that the 3D half-mass radius, r_{hm}, is equal to the 3D half-light radius, r_{hl}. In this case, we convert the projected half-light radius to the 3D half-light radius by multiplying it with a geometrical factor 4/3, correcting for the projection:

$$r_{hm} = r_{hl} = (4/3)r_{phl}. \tag{7}$$

(ii) Case 2: with a correction for MS.
We assume that the cluster did experience an amount of MS at $t = \tau_{obs}$ in the form of a constant conversion factor between the projected half-light radius, r_{phl}, and the 3D half-mass radius, r_{hm}, which we read off from fig. 4 of Hurley (2007):

$$r_{hm} = c_{ms}r_{phl}, \tag{8}$$

with $c_{ms} = 1.9$ for clusters with ages >7 Gyr and $c_{ms} = 1.8$ for a cluster ~4 Gyr of age. Note that this conversion includes the geometric conversion factor of 4/3 and a factor ~1.425, respectively, ~1.35 to account for MS.

By doing this, we can compare the observational half-mass radii to the half-mass radii from the simulations. See the third and fourth column of Table 2 for the calculated observational half-mass radii without and with a correction for MS, respectively.

2.4 Confidence regions

After a simulation we obtain sets of initial conditions, final conditions and their corresponding posterior probabilities for n clusters. This also includes proposed sets of initial conditions, even if these were eventually rejected. From these n initial conditions, we remove the initial conditions from the initialization, from the burn-in and those outside the ranges given in equation (3). Hence, we have each particular initial condition appear only once in our data. The remaining initial conditions include those that survive until $t = \tau_{obs}$ and those that dissolve before reaching the observed cluster's age. Besides analysing the most probable regions in initial total mass versus initial half-mass radius, we namely also want to study the regions that are not suitable for producing the currently observed clusters.

Of the surviving initial conditions, we determine the regions with a 68.3 and 99.7 per cent confidence level: (1) we calculate the normalized posterior probability of each of the sets of initial conditions by dividing the posterior probability of each set by the sum of all the
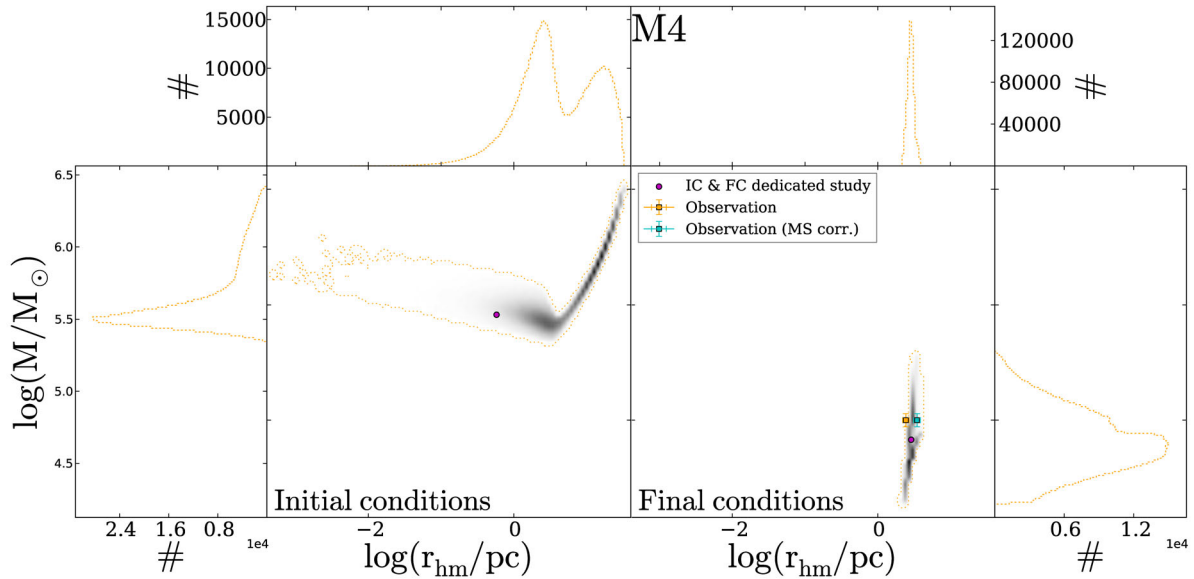
Figure 2. A simple example of the results for the cluster M4. Initial and final condition distributions in half-mass radius versus total mass, where the three panels on the left show the initial conditions and the three panels on the right show the final conditions. The square panels show the two-dimensional histograms in $\log(M)$ versus $\log(r_{hm})$ of the 99.7 per cent confidence region of the simulations that fit the observables without a correction for MS in a black–white density plot: the darker the area, the more initial conditions were sampled in this area. Overplotted on these two-dimensional histograms are the outer contours of the two-dimensional histograms of the 99.7 per cent (yellow dotted line) confidence level initial conditions for both the simulations without a correction for MS, with the projected histograms for $\log(r_{hm})$ at the top and for $\log(M)$ on the left, respectively, right-hand side. The yellow square with error bars show the observation of the cluster's current mass and half-mass radius when no correction for MS is made, and the cyan square with error bars shows the observable with a correction. The pink filled circle in the left-hand panel denotes the initial condition used by the DS, which evolves to the final condition shown by the pink filled circle in the right-hand panel.

posterior probabilities; (2) from the set of initial conditions with the highest normalized posterior probability downwards, we sum the normalized posterior probabilities of each subsequent set of initial conditions until this sum equals 0.997 (0.683). The sets of initial conditions included in that sum are a subset of initial conditions that make up 99.7 per cent (68.3 per cent) of the total posterior probability, i.e. the 99.7 per cent (68.3 per cent) confidence region. Note that our definition of the 99.7 per cent confidence region is different from what is usually meant with a 99.7 per cent confidence region, namely the region containing 99.7 per cent of all the data points. The reason for our alternative definition is that our aim is to show those regions of initial conditions with high posterior probability and if we were to use 99.7 per cent of all the data points, this region would contain a large number of initial conditions with low posterior probability ($p < 0.01$).

In Fig. 2, we show a simple example of our results for the cluster M4 without a correction for MS, whereby the 99.7 per cent confidence region in both the initial and the final conditions are enclosed by the yellow, dotted contours.

3 VALIDATION

3.1 Validation strategy

We validate our method by applying it to nine star clusters that have been studied to great extent with either *N*-body simulations or Monte Carlo methods. These nine clusters include one Galactic open cluster, seven Galactic globular clusters and one extragalactic globular cluster; see Table 1 for the names of the clusters, the cluster types, their host galaxy, the references to papers in which these clusters were studied and with which simulation technique.

3.1.1 Direct comparison

The first step in the validation is to do a direct comparison of the cluster evolution codes by starting from the same sets of initial conditions and evolving the cluster under conditions which are as similar as possible. Therefore, for each cluster we start at the (best-fitting) set of initial condition put forward by the dedicated studies (DSs) and we evolve this cluster up to the same age under similar conditions, which we describe in Section 3.2 and summarize in Table 2.

3.1.2 Independent EMACSS-MCMC runs

The second step is to run our EMACSS-MCMC method (Section 2.2) independently and determine which initial masses and half-mass radii reproduce the cluster observables best, explore possible degeneracies therein and observe whether the best-fitting initial conditions of the DS are contained within our confidence regions. For the sake of comparison to the mentioned DSs, we adopt the cluster observables that were used in the references mentioned in Table 1, even though some cluster parameters are presently better constrained by more recent studies, see e.g. table 1 of the recent study of Marks & Kroupa (2010), where present-day masses and half-mass radii are listed for a number of clusters. Our goal in this paper is to validate our method by comparing our results to the results which were obtained with the DSs. Therefore, it is more important to adopt the observables from these studies than to use the currently best constrained observables. See Section 3.2 and Table 2.

The next step is to exploit the power of MCMC. In the five-dimensional version of our EMACSS-MCMC method, we add the galactocentric distance, age and orbital velocity as nuisance parameters

Table 1. The nine star clusters on which we apply our method to validate it. The first column lists the name of the cluster, the second column the cluster type and the third column the galaxy in which the cluster resides. The fifth column shows the references to the studies which already studied these clusters to great extent with the simulation technique mentioned in column four. The clusters are mentioned in the order of increasing current half-mass relaxation time that was taken from the Harris Catalogue (Harris 2010), except for the first and last mentioned cluster, where we took the relaxation times from the corresponding reference in this table. See Table 2 for the values of these relaxation times.

Name	Cluster type	Galaxy	Simulation technique	Reference
M67	Open cluster	Milky Way	Direct *N*-body	Hurley et al. (2005)
NGC 6397	Globular cluster	Milky Way	Monte Carlo	Giersz & Heggie (2009)
M4	Globular cluster	Milky Way	Monte Carlo	Heggie & Giersz (2008)
M22	Globular cluster	Milky Way	Monte Carlo	Heggie & Giersz (2014)
Palomar 4	Globular cluster	Milky Way	Direct *N*-body	Zonoozi et al. (2014)
47 Tuc	Globular cluster	Milky Way	Monte Carlo	Giersz & Heggie (2011)
Palomar 14	Globular cluster	Milky Way	Direct *N*-body	Zonoozi et al. (2011)
ω Cen	Globular cluster	Milky Way	Monte Carlo	Giersz & Heggie (2003)
G1	Globular cluster	M31	Scaled *N*-body	Baumgardt et al. (2003b)

Table 2. Observational data of the validation clusters as used in the references mentioned in Table 1. The first column lists the cluster name and the second column the observed mass in $10^4\,M_\odot$. The third and fourth columns lists the half-mass radius without a correction for MS (i.e. equal to the 3D half-light radius) and the half-mass radius with a correction for MS, respectively. The galactocentric radius, age, orbital velocity of each cluster as used in the references mentioned in Table 1 are listed in column five, six and seven, respectively. For the sake of comparison to these DSs, we use these observables in our simulations, even though some cluster parameters are presently better constrained by more recent observations. See Section 3.2 for the reasoning behind choosing each of these parameter values.

Name	$M_{\rm obs}$ $(10^4\,M_\odot)$	$r_{\rm hm,\,obs}$ (pc)	$r_{\rm hm,\,obs}$ (MS corr.) (pc)	$R_{\rm GC,\,obs}$ (kpc)	$\tau_{\rm obs}$ (Gyr)	$v_{\rm obs}$ (km s^{-1})	$\log(t_{\rm rh})$ (yr)
M67	0.14	3.35	4.52	8.0	4	220	8.48
NGC 6397	6.6	2.30	3.28	1.99	12	220	8.6
M4	6.3	2.43	3.47	1.68	12	220	8.93
M22	33	4.17	5.94	5.28	12	220	9.23
Pal 4	2.98	24.7	35.2	102.8	11	200	9.42
47 Tuc	110	4.87	6.94	2.95	12	220	9.55
Pal 14	1.1725	35.4	50.2	71.6	11	220	10.02
ω Cen	390	9.89	14.09	1.22	12	220	10.09
G1	1500	17.6	25.08	–	12	–	10.7

and determine the most probable initial masses and half-mass radii. By comparing this to the results of the two-dimensional runs explained above, we can explore how dependent probable initial masses and half-mass radii are on the choice of the galactocentric radius, $R_{\rm GC}$, age, τ, and velocity, v. Adding these parameters as nuisance parameters is observationally motivated, since all observables are always determined with some error. The method here is similar to the description in Section 2.2, but the difference is that now at each iteration we also sample a galactocentric radius, an age and an orbital velocity from Gaussian distributions with the mean equal to $R_{\rm GC,\,obs}$, $\tau_{\rm obs}$ and $v_{\rm obs}$, respectively, as adopted from the references mentioned in Table 1, see Table 2, and a standard deviation equal to 10 per cent of the mean. For G1, though, we take $R_{\rm GC,\,obs} = 40$ kpc as mentioned in Baumgardt et al. (2003b) and $v_{\rm obs} = 230$ km s^{-1}. We perform our 5D runs only without a correction for MS.

The final step is to investigate the stability of our determined initial conditions against errors in the observed data. We do this in two ways. We first compare our 2D. The second thing we do, is checking how increasing/decreasing the error bars on the fitting parameters ($\log(M)$ and $r_{\rm hm}$) will affect the distribution of initial conditions. The second thing we do, is testing the stability of the initial conditions against varying the parameters $R_{\rm GC}$, v and τ within their

error bars, assuming that the observed mass and half-mass radius are unchanged. We take 10 per cent errors and look at the maximum difference, e.g. comparing a simulation with $R_{\rm GC} = R_{\rm GC,\,obs}$ to simulations with $R_{\rm GC} = R_{\rm GC,\,obs} + 0.1R_{\rm GC,\,obs}$ and $R_{\rm GC} = R_{\rm GC,\,obs} - 0.1R_{\rm GC,\,obs}$, respectively.

3.2 Validation clusters

3.2.1 *ω Centauri, M4, NGC 6397, 47 Tucanae and M22*

In this section, we describe the studies using the Monte Carlo code MOCCA (Giersz 1998, 2001, 2006) modelling five Galactic globular clusters: ω Cen (NGC 5139; Giersz & Heggie 2003), M4 (NGC 6121; Heggie & Giersz 2008), NGC 6397 (Giersz & Heggie 2009), 47 Tuc (NGC 104; Giersz & Heggie 2011) and M22 (NGC 6656; Heggie & Giersz 2014). Hereafter, we refer to these five studies as GH03-14.

Simulation Technique. For each of the globular clusters GH03-14 determined a set of initial conditions – and a few sets of initial conditions in the case of M22 – by means of small-scale modelling, i.e. by performing simulations for clusters with a lower initial number of stars. These initial conditions were subsequently evolved up to

the age of the cluster, which was taken to be 12 Gyr for each of these clusters. For M4, NGC 6397, 47 Tuc and M22 their simulations included prescriptions for single and binary stellar evolution, for the Galactic tidal field, for two-body relaxation and for binaries and their dynamical interactions. For ω Cen, which was studied with an early version of MOCCA, their simulation included simple prescriptions for single stellar evolution and for the dynamical evolution in the Galactic tidal field. After evolution these clusters gave a satisfactory match to a number of observed characteristics, such as the surface brightness profile and the velocity dispersion profile. See the references mentioned in Section 3.2.1 for the details of their MOCCA code.

Orbit and tides. GH03–14 evolved each of these clusters on a circular orbit with a circular velocity of 220 km s^{-1}.[5] They set the tides by imposing an initial tidal radius, $r_{t, i}$. Given this tidal radius and their initial total cluster mass, M, and assuming an isothermal model for the Galaxy, we calculate per cluster with which Galactocentric radius, R_{GC}, their model is consistent by combining equations (1) and (2). We use these Galactocentric radii as input for our simulations, see the fifth column of Table 2.

They evolved their model clusters with an initial tidal radius of 35, 86, 40, 89 and 90 pc, which are consistent with a Galactocentric radius of 1.68, 2.95, 1.99, 5.28 and 1.22 kpc for the clusters M4, 47 Tuc, NGC 6397, M22 (we compare to their model B, see table 1 of Heggie & Giersz 2014) and ω Cen, respectively. Given the fact that M4 is on an eccentric orbit with (eccentricity e, perigalacticon R_p/kpc, apogalacticon R_a/kpc) of about (0.8, 0.6, 5.9; Dinescu, Girard & van Altena 1999), this cluster experiences strong tides near perigalacticon. Therefore their choice of the initial tidal radius, and its corresponding galactocentric radius, are very reasonable and better than evolving the cluster at its current Galactocentric radius of 5.9 kpc (Harris 2010): the averaged tidal field experienced by their cluster during its 12 Gyr circular orbit with a Galactocentric radius of 1.68 kpc is comparable to the tidal field experienced by M4 in its actual eccentric orbit. Their choices for the initial tidal radii for NGC 6397 and M22 with (e, R_p, R_a) of about (0.34, 3.1, 6.3) and (0.53, 2.9, 9.3), respectively, (Dinescu et al. 1999) are also reasonable, but their choices for ω Cen and 47 Tuc with (e, R_p, R_a) of about (0.67, 1.2, 6.2) and (0.17, 5.2, 7.3), respectively, are slightly overestimating the effect of the tidal field. However, in order to have a good comparison to the studies mentioned above, for each of these clusters we evolve all our model clusters on a circular orbit with a circular velocity of 220 km s^{-1} at the Galactocentric radius to which these models are consistent with, see Table 2.

Observed mass and radius. GH03–14 get the observational mass of M4 of 6.3×10^4 M$_\odot$ from Richer et al. (2004) and got the observed half-light radius from Harris (1996), which in turn lists angular half-mass radii, stated to be taken from the direct average of Trager, King & Djorgovski (1995) and van den Bergh, Morbey & Pazder (1991). Since both latter studies obtain their half-light radii from projected data, we assume that Harris (1996) used a one-to-one relation between half-light radii and half-mass radii, since Harris (2010) lists half-light radii and these values are in many cases very similar to the in Harris (1996) mentioned 'half-mass radii'. The 2.3 pc for the half-light radius mentioned in table 2 of Heggie & Giersz (2008) is a mistyped value (Heggie, private communication), since the angular projected half-light radius θ_{phl} given in Harris (1996) is 3.65 arcmin (see also table 1 of Giersz &

Heggie 2009). In combination with the distance between M4 and the Earth, $R_E = 1.72$ kpc mentioned in Heggie & Giersz (2008), θ_{phl} converts to $r_{phl} = 1.83$ pc using equation (6). We therefore use $r_{phl} = 1.83$ pc; for the conversion to the 3D half-mass radius r_{hm} with a correction for MS (see Section 2.3), we use the relation (8) with $c_{MS} = 1.9$.

GH03–14 got the observational mass for 47 Tuc of 1.1×10^6 M$_\odot$ from Meylan (1989), for NGC 6397 of 6.6×10^4 M$_\odot$ from Drukier (1995) and for ω Cen of 3.9×10^6 M$_\odot$ from Pryor & Meylan (1993). They do not mention the observational cluster mass of M22, so we take the cluster mass of 3.3×10^5 M$_\odot$ from Richer et al. (2008). GH03–14 got the observed radius for 47 Tuc of 2.79 arcmin and for NGC 6397 of 2.33 arcmin both from Harris (1996); they do not mention the observational radius for ω Cen and M22, so we get the observed radius for ω Cen of 5.00 arcmin from Harris (1996) and for M22 of 3.36 arcmin from Harris (2010), respectively. Using the same reasoning as mentioned for M4, we assume the mentioned observed radii to be the projected (2D) angular half-light radii θ_{phl}. We calculate r_{phl} in by using equation (6) in combination with distances of 47 Tuc, NGC 6397, ω Cen and M22 to the Earth, R_E, of 4.5 kpc (Giersz & Heggie 2011), 2.55 kpc (Giersz & Heggie 2009), 5.1 kpc (Harris 1996) and 3.2 kpc (Harris 2010), respectively. For the conversion to the 3D half-mass radius r_{hm} with a correction for MS, we use the relation (8) with $c_{MS} = 1.9$.

Model initial and final conditions. The best-fitting sets of initial conditions GH03–14 found for NGC 6397, M4, 47 Tuc and M22 (model B) in (mass/ M$_\odot$, half-mass radius/pc) are listed in Table 3. For ω Cen Giersz & Heggie (2003) mention the initial and final mass of their best-fitting model (we list those in Table 3), but they do not mention the initial and final half-mass radii of that model, only their initial and final tidal radii. Assuming that the tidal radius is the edge radius of the King model initially (Heggie, private communication), we can calculate the initial half-mass radius by using the ratio of tidal-to-half-mass radius taken from fig. 8.3. in Heggie & Hut (2003). Using $r_t/r_{hm} \sim 9.65$ for a central potential $W_0 = 7.7$, we find $r_{hm, i} = 9.33$ pc. It is not clear whether this assumption is still valid after 12 Gyr of evolution, so we cannot calculate their final half-mass radius.

3.2.2 Palomar 14 and Palomar 4

In this section, we describe the first published direct *N*-body simulations of the two large and sparse Galactic globular clusters, both residing in the outer halo: Pal 14 (Zonoozi et al. 2011) and Pal 4 (Zonoozi et al. 2014). They use the collisional *N*-body code NBODY6 (Aarseth 2003) on Graphics Processing Unit (GPU) computers. Hereafter, we refer to these two studies by Z11–14.

Simulation Technique. Z11–14 simulate the evolution of Palomar 14 and Palomar 4 and for Pal 14 they compute 65 models and for Pal 4 a total of 20 models, divided in three categories: 1) clusters with a Kroupa (2001) IMF in the range $0.08 < M/M_\odot < 100$ (referred to as their *canonical-NS* model), (2) clusters with a flattened IMF, (3) clusters with a Kroupa (2001) IMF, but with primordial MS. For Pal 14 they computed one additional model with a Kroupa (2001) IMF, but with primordial binaries. See the references mentioned in Section 3.2.2 for the details of their simulations.

Orbit and tides. For Pal 14, Z11–14 varied the initial half-mass radius and mass and evolved each cluster for 11 Gyr on a circular orbit in a logarithmic potential with a circular velocity of 220 km s^{-1} at Palomar 14's currently observed Galactocentric radius, of which the authors do not mention the value they adopted. After the

---

[5] Giersz & Heggie (2003) do not mention which circular velocity they adopted, but we assume it was a value of 220 km s^{-1} as well.

Table 3. Results for the validation in three significant figures. For each validation cluster mentioned in the first column, seven parameters are compared between the observation in the first subrow, the best-fitting results of the DS (see Table 1 for the references) in the second subrow, EMACSS' result from the initial condition of the DS in the third subrow, EMACSS-MCMC' best-fitting results without and with a correction for MS in subrows four and five, respectively (see Section 2.3). The parameters are the initial number of stars N_i in column three, the initial mass M_i (in $10^5 \, M_\odot$) in column four, the initial half-mass radius $r_{hm, i}$ (in pc) in column five, the final number of stars N_f in column six, the final (current) mass M_f (in $10^4 \, M_\odot$) in column seven, the final (current) half-mass radius $r_{hm, f}$ (in pc) in column eight and the question whether MS has occurred in column nine. The observed value for the current half-mass radius in column eight shows two values: the first one without a correction for MS and the second one with a correction for MS, see Section 2.3 and Table 2.

Cluster	Source	N_i	M_i $(10^5 \, M_\odot)$	$r_{hm, i}$ (pc)	N_f	M_f $(10^4 \, M_\odot)$	$r_{hm, f}$ (pc)	CC?[a]
M67	Observation	–	–	–	–	0.140	3.35/4.52	–
	DS	36.0 k	0.187	3.90	3.52 k	0.204	3.80	No
	EMACSS from IC of DS	29.2 k	0.187	3.90	19.0	0.820	6.51	No
	EMACSS best fit	25.2 k	0.162	0.006	2.64	0.141	3.39	Yes
	EMACSS best fit (MS corr.)	347 k	2.22	43.0	2.39	0.149	4.49	No
NGC 6397	Observation	–	–	–	–	6.60	2.31/3.29	Yes
	DS	–	3.65	0.400	–	6.03	3.22	Yes
	EMACSS from IC of DS	570 k	3.65	0.400	143 k	7.28	3.21	Yes
	EMACSS best fit	1.21 M	7.77	$1.18 \cdot 10^{-4}$	102 k	4.40	2.89	Yes
	EMACSS best fit (MS corr.)	435 k	2.79	2.78	138 k	6.60	3.29	Yes
M4	Observation	–	–	–	–	6.30	2.44/3.48	No
	DS	485 k	3.40	0.580	86.0 k	4.61	2.89	Yes
	EMACSS from IC of DS	531 k	3.40	0.580	79.1 k	4.54	2.69	Yes
	EMACSS best fit	1.20 M	7.66	1.19×10^{-3}	121 k	5.87	2.78	Yes
	EMACSS best fit (MS corr.)	495 M	3.17	4.08	125 k	6.28	3.48	No
M22	Observation	–	–	–	–	33.0	4.17/5.95	No
	DS	832 k	5.70	2.72	–	32.0	6.60	No
	EMACSS from IC of DS	891 k	5.70	2.72	811 k	29.9	6.28	No
	EMACSS best fit	1.17 M	7.50	0.358	849 k	33.1	4.19	Yes
	EMACSS best fit (MS corr.)	978 k	6.26	2.53	898 k	33.1	5.95	No
Pal 4	Observation	–	–	–	–	2.98	24.5/35.0	No
	DS	100 k	0.500–0.570	12.0–14.5	–	2.68–3.24	23.2–27.6	No–no
	EMACSS from IC of DS	78.1–87.3 k	0.500–0.570	12.0–14.5	76.5–87.2 k	2.78–3.18	26.6–31.1	No
	EMACSS best fit	83.7 k	0.535	10.9	82.1 k	2.98	24.5	No
	EMACSS best fit (MS corr.)	83.8 k	0.536	16.6	81.9 k	2.98	35.0	No
47 Tuc	Observation	–	–	–	–	110	4.87/6.94	No
	DS	2.04 M	16.4	1.91	1.87 M	90.0	4.96	No
	EMACSS from IC of DS	2.56 M	16.4	1.91	2.38 M	87.4	4.57	No
	EMACSS best fit	3.19 M	20.4	2.04	3.01 M	110	4.87	No
	EMACSS best fit (MS corr.)	3.22 M	20.6	3.12	3.00 M	110	6.93	No
Pal 14	Observation	–	–	–	–	1.1725	35.2 / 50.2	No
	DS	70.0–100 k	0.400–0.600	15.0–25.0	–	1.86–2.89	26.1–42.8	–
	EMACSS from IC of DS	62.5–93.8 k	0.400–0.600	15.0–25.0	59.4–87.9 k	2.17–3.22	31.5–47.9	No–no
	EMACSS best fit	35.6 k	0.228	17.6	31.5 k	1.17	35.2	No
	EMACSS best fit (MS corr.)	136 k	0.869	64.1	56.2 k	2.11	49.3	No
ω Cen	Observation	–	–	–	–	390	9.89/14.1	No
	DS	–	110	9.33	–	360	–	No
	EMACSS from IC of DS	17.2 M	110	9.33	15.7 M	570	16.5	No
	EMACSS best fit	11.7 M	74.7	5.14	10.6 M	390	9.89	No
	EMACSS best fit (MS corr.)	11.9 M	76.2	7.84	10.7 M	390	14.1	No
G1	Observation	–	–	–	–	1.50×10^3	17.6/25.1	–
	DS	–	127	3.86	–	760	6.76	No
	EMACSS from IC of DS	19.8 M	127	3.86	19.8 M	713	8.5	No
	EMACSS best fit	41.7 M	267	9.20	41.7 M	1.50×10^3	17.6	No
	EMACSS best fit (MS corr.)	41.7 M	267	13.5	41.7 M	1.50×10^3	25.1	No

[a]The results whether a cluster had undergone core-collapse according to observations are taken from Trager et al. (1995), except for G1, where we adopt what Baumgardt et al. (2003b) argued about the core-collapse state of these two clusters.
[b] The authors studying this cluster with their dedicated study find multiple initial conditions; we only list their first model here.

evolution, they fit the final values for the number of bright stars, the projected half-light radius and the slope of the mass function in the mass range 0.525–0.795 $M_{\odot}$ to the observed ones. To make a fair comparison, we also evolve all of our model clusters for Pal 14 on a circular orbit at its current Galactocentric radius, for which we adopt a value of 71.6 kpc from Harris (2010) with a circular velocity of 220 km s^{-1}. To the best of our knowledge, there are no references reporting on the orbit of Pal 14. Jordi et al. (2009) mention that the orbit could possibly be eccentric, in which case evolving the cluster on a circular orbit at the current Galactocentric radius is an underestimation of the tidal field.

For Pal 4, Z11–14 also varied the initial half-mass radius and mass and evolve each cluster for 11 Gyr on a circular orbit with a circular velocity of 200 km s^{-1} at Palomar 4's current Galactocentric radius of 102.8 kpc in an analytic Galactic background potential consisting of a bulge, a disc and a logarithmic halo, which they adjusted to resemble the Milky Way.

Observed mass and radius. Z11–14 got the observed total mass for Pal 14 of about 12000 $M_{\odot}$ from Jordi et al. (2009) and for Pal 4 of about 29 800 $M_{\odot}$ from Frank et al. (2012). For Pal 14, Z11–14 got the observed projected angular half-light radius θ_{phm} of 1.28 arcmin from Hilker (2006), which they in turn convert to the projected (2D) half-light radius r_{phl} of 26.4 ± 0.5 pc and a 3D half-light radius r_{hl} of 35.4 ± 0.6 pc. For Pal 4, Z11–14 got the observed projected angular half-light radius θ_{phm} of 0.62 arcmin from King (1966) model fitting on Wide Field Planetary Camera 2 (WFPC2) data and broad-band imaging with the Low-Resolution Imaging Spectrometer at the Keck II telescope, which they convert to the projected (2D) half-light radius r_{phl} of 18.4 ± 1.1 pc and a 3D half-light radius r_{hl} of about 24 pc. We converted these projected half-light radii to the 3D half-mass radii r_{hm} with a correction for MS (see Section 2.3) by using the relation (8) with $c_{MS} = 1.9$.

Model initial and final conditions. For both Pal 14 and Pal 4, we compare to their canonical-NS models, since these models are most comparable to EMACSS. For Pal 14, these are the 28 models mentioned in table 1 of Zonoozi et al. (2011) with initial masses in the range 40 000–60 000 $M_{\odot}$ (Zonoozi, private communication) and initial half-mass radii in the range 15–25 pc. For Pal 4, these are the seven models mentioned in table 1 of Zonoozi et al. (2014) with initial masses in the range 50 000–57 000 $M_{\odot}$ and initial half-mass radii in the range 12–14.5 pc (Zonoozi, private communication). The fact that these are not their best-fitting models is not a problem for validation purposes. However, in our Figs 10 and 12, showing the results of the independent EMACSS-MCMC runs in 2D, we also plot all the other models of Zonoozi et al. (2011, 2014) to see if their other (including best-fitting) models are contained in our confidence regions.

3.2.3 G1

In this section, we describe the study using scaled *N*-body modelling to investigate the evolution of M31's largest globular clusters G1 (Mayall II; Baumgardt et al. 2003b). They use the collisional *N*-body code NBODY4 (Aarseth 1999) on the GRAPE-6 computers (Makino et al. 2003).

Simulation Technique. Baumgardt et al. 2003b simulate the evolution of G1 by running simulations for star clusters with $N = 65\,536$ stars, since direct *N*-body simulations with a number of stars similar to the number of stars present in G1 ($N \sim 10^7$ according to Baumgardt et al. 2003b) was, and still is, out of reach. They used the same half-mass relaxation time t_{rh} for their model as was inferred for G1

from observations (Meylan et al. 2001 estimated $t_{rh} \sim 50$ Gyr). They perform several dozen of runs to determine their best fit to the surface density, velocity dispersion, rotation and ellipticity profiles. Baumgardt et al. (2003b) constructed two models: (1) a single non-rotating cluster, and (2) a rotating merger product, where the merger occurred during the formation process. They varied the initial density profiles, half-mass radii, total masses, and global mass-to-light ratios M/L and evolve each cluster for 13 Gyr. The authors construct the final density and velocity profiles from 10 snapshots in the range 11.75–12.25 Gyr and give their final cluster mass and half-mass radius at 12 Gyr. They use a Kroupa (2001) mass function in the range $0.1 < M/M_{\odot} < 30$ and include the effects of stellar evolution and two-body relaxation. Their simulations do not contain primordial binaries, as G1 should still be far from core-collapse. See the reference mentioned in Section 3.2.3 for the details of their simulation.

Orbit and tides. Baumgardt et al. (2003b) do not include a tidal field, since they argue that the tides would have a negligible effect on the cluster's evolution, since the cluster is currently at a distance of 40 kpc to the centre of M31 (Meylan et al. 2001). We therefore evolve all our model clusters for G1 for 12 Gyr without including a tidal field (i.e. as an isolated cluster); see Table 2.

Observed mass and radius. Baumgardt et al. (2003b) got a set of observed half-mass radii r_{hm} in the range 12.3–15.0 pc and observed total masses in the range 7.3–17 × 10^6 $M_{\odot}$ from Meylan et al. (2001), who in turn estimated the half-mass radii and masses from the surface brightness profile from *Hubble Space Telescope*/WFPC2 images and velocity dispersion profile from KECK/HIRES (High Resolution Echelle Spectrometer) spectra in combination with King model, King–Michie model and virial theorem estimates. We choose to compare our results to the observables which they obtain with their King–Michie model nr 4, which gives somewhat average values of the above mentioned ranges: $r_{hm} = 13.2$ pc, M = 15 × 10^6 $M_{\odot}$ and $t_{rh} \sim 50$ Gyr. However, we have checked that the 'half-mass radius' mentioned in Meylan et al. (2001) comes from their angular projected radii in arcmin by using equation (6) in combination with its distance to the Earth $R_E = 770$ kpc, which they provided in their Table 1. They do not mention that they corrected for projection (factor 4/3) or that they did any correction for MS. We therefore assume that the radius they refer to as the half-mass radius is actually the projected half-light radius. For the conversion to the 3D half-mass radius r_{hm} with a correction for MS (see Section 2.3), we use the relation (8) with $c_{MS} = 1.9$.

Model initial and final conditions. For G1, we compare to their non-rotating model, since this model is most comparable to EMACSS. After scaling up, the cluster of this model obtained a final mass of 7.6 × 10^6 $M_{\odot}$ and a final half-mass radius of 6.76 pc (Baumgardt et al. 2003b). They found that during the evolution the cluster mainly expanded by a factor of 1.75 due to stellar evolution and that it lost about 40 per cent of its mass over 12 Gyr (Baumgardt, private communication). From this, we calculated an initial mass of 1.27 × 10^7 $M_{\odot}$ and an initial half-mass radius of 3.86 pc.

3.2.4 M67

In this section, we describe the work using direct *N*-body modelling to study the evolution of the rich and relatively old Galactic open cluster M67 (NGC 2682; Hurley et al. 2005). The authors simulate the evolution of M67 by using the collisional *N*-body code NBODY4 (Aarseth 1999) on the GRAPE-6 computers (Makino et al. 2003).

Simulation Technique. Hurley et al. (2005) modelled the evolution of M67 by performing *N*-body simulations. They compared their modelled surface density profile to the surface density profile of M67 of Bonatto & Bica (2005) provided by Bonatto (private communication), their modelled colour–magnitude diagram (CMD) to the observed CMD of Montgomery, Marschall & Janes (1993) and their modelled luminosity function and their structural parameters such as the half-mass radius to the observational data from Fan et al. (1996). They furthermore extensively study the stellar populations in their simulation and especially focus on the formation channels of blue stragglers (BSs) and compare their results to observational data from Fan et al. (1996), Latham & Milone (1996), Milone & Latham (1992) and Leonard (1996). For the single stars, they use a Kroupa, Tout & Gilmore (1993) mass function in the range $0.1 < M/M_\odot < 50$ and their model fully accounts for the effects of cluster dynamics as well as stellar and binary evolution, including a significant fraction of primordial binaries. Hurley et al. (2005) constructed two different models, differing only in the initial mass, the Galactocentric radius and the binary period distribution. Their second and favoured colour model are ran for a star cluster with $N = 36\,000$ stars. See Hurley et al. (2005) for the details of their models and the *N*-body code they used.

Orbit and tides. We compare to the second model of Hurley et al. (2005), because it is their best-fitting model. In this model, they evolved the cluster for 4 Gyr on a circular orbit with a circular velocity of 220 km s^{-1} at a Galactocentric radius of 8.0 kpc, which is a reasonable choice for a cluster on an slightly eccentric orbit with a perigalacticon of 6.8 kpc and a apogalacticon of 9.1 kpc (Carraro & Chiosi 1994).

Observed mass and radius. The half-mass radius of main-sequence stars observed within 10 pc that Hurley et al. (2005) used was taken from Fan et al. (1996), who determined it to be 2.5 pc. However, we checked that the 'half-mass radius' mentioned in Fan et al. (1996) comes from converting their angular projected radii in arcmin by using equation (6) in combination with the cluster's distance to the Earth, $R_E = 783$ pc, calculated from their provided distance modulus of 9.47 mag. They do not mention that they corrected for projection (factor 4/3) or that they did any correction for MS. We therefore assume that the radius they refer to as the half-mass radius, is actually the projected half-light radius. For the conversion to the 3D half-mass radius r_{hm} with a correction for MS (see Section 2.3), we use the relation (8) with $c_{MS} = 1.8$. Both studies took the total luminous cluster mass from Fan et al. (1996), which determined that to be $1000\,M_\odot$. Hurley et al. (2005) estimated that this luminous mass represented a total cluster mass of about $1400\,M_\odot$.

Model initial and final conditions. The best-fitting initial conditions Hurley et al. (2005) found for M67 (model 2) in (mass/$M_\odot$, half-mass radius/pc) are listed in Table 3.

4 RESULTS

4.1 Performance

In this section, we test the performance of the EMACSS-MCMC method. We first determined a suitable number of the walkers, n_w, burn-in iterations, n_b, and subsequent chain iterations, n_c, such that we have a good balance between proper coverage and quick convergence. To this end, we ran a dozen simulations for the cluster M4 varying these three numbers and plotting the posterior probability of an iteration as a function of the iteration number. We divided all the iteration in bins of 50 iterations and calculated the minimum, maximum and

mean probability per bin, see Fig. 3. In these simulations, we used a prior distribution that is uniform in mass (similar to the first line of equation 3), but semi-uniform in half-mass radius: the upper limit of the half-mass radius is mass-dependent through the dependence on the Jacobi radius, r_J:

$$\log(M_{obs}) \leq \log\left(\frac{M}{M_\odot}\right) \leq \log(M_{obs}) + 3,$$
$$0 < \frac{r_{hm}}{pc} < 0.3 r_J. \tag{9}$$

This mass-dependent upper limit of the initial half-mass radius is motivated by the fact that most clusters with initial half-mass radii larger than 30 per cent of the Jacobi radius will quickly dissolve (Alexander et al. 2014). As we show later on in this section, initializing the walkers according to this prior does not exclude the parameter space with $r_{hm}/r_J > 0.3$, but it does accelerate the convergence.

In order to judge whether the walkers have converged, we look at the instance that both the maximum and the mean posterior probability have stabilized, which means that its value does not increase or decrease by a significant amount, say 100 per cent, and thus only show the variation caused by the scatter. The scatter in the mean posterior probability is a natural feature of any MCMC sampler, because it is important that even though a (local) maximum in posterior probability has been found, the walkers continue to explore other regions of parameter space, in order to locate possible other maxima.

From the first row of Fig. 3, showing the simulation with (n_w, n_b, n_c) = (20, 100, 100), we see that the walkers already start to converge after about 2000 iterations, marking the end of the burn-in phase. However, from the right-hand column of the first row, we see that the coverage of the M–r_{hm} plane is still poor, meaning that we can observe by eye that the two-dimensional parameter space is not well-sampled and/or that the sampled region does not cover a large region of that parameter space. In the second row of Fig. 3, we see that both convergence and proper coverage, by eye, seem to have been established for the simulation with (n_w, n_b, n_c) = (50, 100, 1000): the walkers probed a wide range of initial masses and half-mass radii in proposing initial conditions. Nevertheless, we have chosen to be conservative and to use (n_w, n_b, n_c) = (50, 100, 1000) only for *test simulations*[6] and to use (n_w, n_b, n_c) = (100, 1000, 10000) for all main simulations in this work, see the third row of Fig. 3.

We secondly determined whether the choice of a prior distribution would affect the ranges of parameter space that are covered and thus the determined probable initial condition distribution. To test this, we ran three simulations to determine the initial conditions for the cluster M4 with (n_w, n_b, n_c) = (50, 100, 1000) using three different priors, but otherwise being the same. These three priors were

(1) a uniform distribution in both (logaritmic) mass and half-mass radius, according to equation (3);

(2) a normal distribution in both parameters with the mean equal to $\log (M_{obs})$ and $r_{hm, obs}$, respectively, and a standard deviation equal to 10 per cent of the mean;

(3) a semi-uniform distribution, according to equation (9).

The results of these three simulations are shown in Fig. 4. From this figure, we can see that the covered area in the M–r_{hm} plane

---

[6] Testing the effect of the prior distribution or observational errors on the determined probable initial condition distributions.
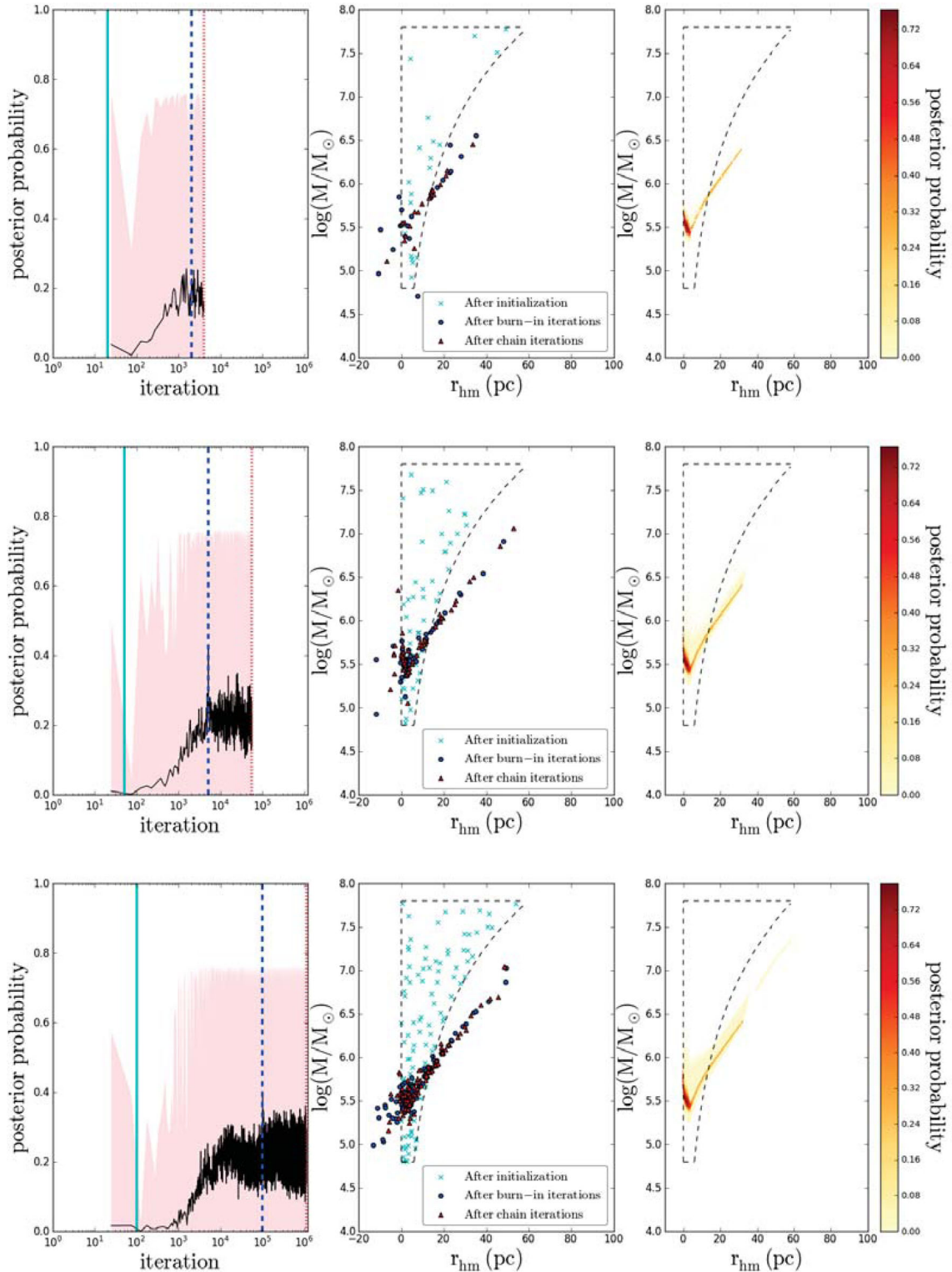
Figure 3. MCMC performance in terms of convergence for the simulation of M4 without a correction for MS. The left-hand column shows the posterior probability of an iteration as a function the iteration number, averaged over bins of 50 iterations. The solid black line shows the mean probability of each bin, the pink area marks the region between the minimum and the maximum probability in each bin and the vertical solid cyan, dashed blue and dotted red lines, mark the phases after initialization, the burn-in phase and the subsequent chain iterations, respectively. The middle column shows the distribution of the walkers after initialization (our prior; cyan crosses), burn-in (blue circles) and the chain iterations (red triangles), respectively. The right-hand column shows the distribution of all the sampled initial conditions with a non-zero posterior probability, colour coded by the value of the posterior probability as indicated by the colour bar. The first row is for the simulation with $(n_{\rm w}, n_{\rm b}, n_{\rm c}) = (20, 100, 100)$, the second row for the simulation with $(n_{\rm w}, n_{\rm b}, n_{\rm c}) = (50, 100, 1000)$ and the third row for the simulation with $(n_{\rm w}, n_{\rm b}, n_{\rm c}) = (100, 1000, 10000)$.
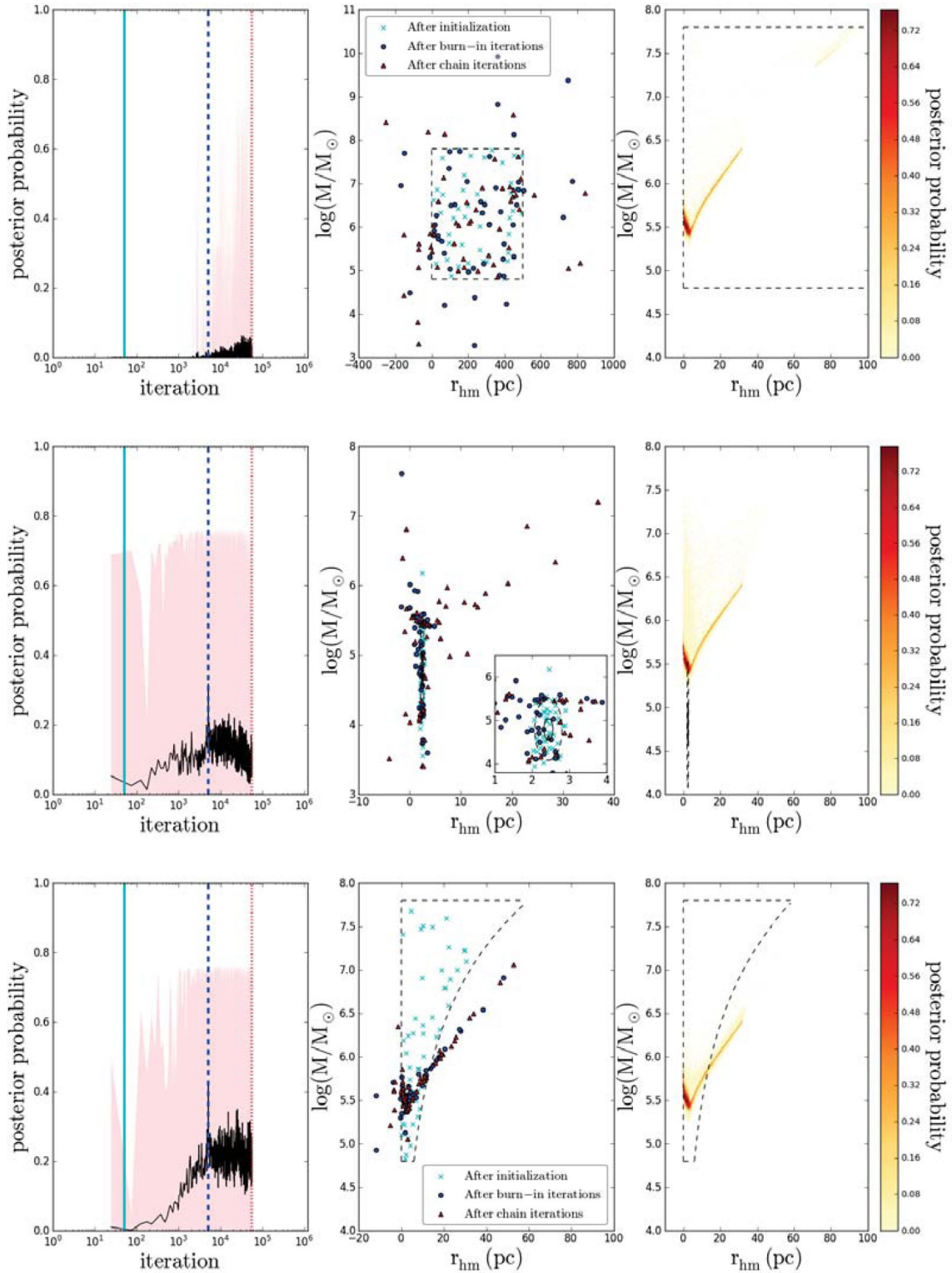
Figure 4. Similar to Fig. 3, but this time showing the dependence of the initial conditions and performance in terms of convergence and coverage on the choice of prior distribution. The top panel shows the performance after choosing a uniform prior distribution indicated by the square box. The middle panel shows the performance after choosing a normal prior distribution, with the current mass and half-mass radius as the mean and a tenth of these values as the standard deviation; see the ellipses indicating the 1σ (solid black line) and the 3σ lines of the prior distribution in the zoomed in smaller panel. The third panel shows the performance after choosing a semi-uniform distribution, i.e. the mass is drawn uniformly between two boundaries, but the radius is dependent on the Jacobi radius, which is mass dependent; see the semi-uniform prior indicated by the black dashed line.

of the probable initial conditions is similar. If we consider all sampled initial conditions (also those outside of the boundaries given by equation 3, e.g. negative half-mass radii, with posterior probabilities equal to zero, which is not shown in Fig. 4), the sampled area is significantly different: the simulation with a uniform prior covers a larger range in initial half-mass radius $(-500 \lesssim (r_{hm,i}/pc) \lesssim 1000)$ and slightly different, but overlapping range in logarithmic mass $(2.0 \lesssim \log(M_i/M_\odot) \lesssim 10.5)$ compared to the semi-uniform prior $(-68.9 \lesssim (r_{hm,i}/pc) \lesssim 150$ and $2.9 \lesssim \log(M_i/M_\odot) \lesssim 9.8)$ and the normal prior $(-26.9 \lesssim (r_{hm,i}/pc) \lesssim 60.4$ and $1.1 \lesssim \log(M_i/M_\odot) \lesssim 9.1)$. If we consider initial conditions with posterior probability greater than zero, then the covered area is slightly more similar: the walkers initialized according to a uniform prior reach larger initial half-mass radii, but the initial mass range is comparable (uniform: $10^{-3} < (r_{hm,i}/pc) < 95.7$ and $5.3 < \log(M_i/M_\odot) < 7.8$; semi-uniform: $10^{-4} < (r_{hm,i}/pc) < 63.8$ and $5.3 < \log(M_i/M_\odot) < 7.8$; normal: $10^{-4} < (r_{hm,i}/pc) < 58.0$ and $5.3 < \log(M_i/M_\odot) < 7.7$). We observe in the top panel of Fig. 4 that there is an area of initial conditions with high initial mass and high initial radius, that is not probed with the simulations with the other two priors. However, this is not a favourable region in terms of posterior probability and thus we conclude that simulations with different prior distributions properly cover the relevant ranges of parameter space and that the derived initial conditions are prior independent. Similar behaviour is seen for the other clusters in our sample. We use the semi-uniform prior distribution for the rest of our simulations in this work.

The final performance characteristic to test is the sampling of initial conditions by the walkers. The results of all the simulations for both the 2D and 5D runs are shown in Figs 6–14, Fig. 15 and Figs A1–A8. By comparing the two-dimensional histograms with the confidence contours in these figures, we see that the most sampled areas overlap with the high posterior probability regions. This is what one would expect for an MCMC method with a sufficient number of iterations, and hence shows the proper performance of our method. We note that the number of sets of initial conditions in the 99.7 and 68.3 per cent confidence regions is less than ∼99.7 per cent, respectively, ∼68.3 per cent, of the total number of surviving initial conditions, and that increasing the number of iterations does not increase these percentages. For instance, for M4 the number of sets of initial conditions in the 99.7 and 68.3 per cent confidence regions is ∼80 per cent, respectively, ∼40 per cent of the total number of surviving initial conditions for both the simulation with $(n_w, n_b, n_c) = (50, 100, 1000)$ and the simulation with $(n_w, n_b, n_c) = (100, 1000, 10000)$. This is again because even though the walkers have converged to high posterior probability regions of parameter space, they continue to sample unexplored regions as well.

4.2 Direct comparison

Fig. 5 shows the direct comparison between EMACSS and the DSs by running EMACSS from their best-fitting initial condition. All results presented in this section are summarized in Table 3, where we compare the best-fitting results of the DS and EMACSS' result when starting from the initial condition of the DS in row two and three for each cluster.

From Fig. 5, we see that the EMACSS results compare quite well to the Monte Carlo and the *N*-body results for NGC 6397, M4, M22, Pal 4, 47 Tuc, Pal 14 and G1, with a difference in final conditions <25 per cent with respect to the DSs in both (linear) mass and half-mass radius for each of these clusters. For M4, M22 and 47 Tuc, we see that the evolution with EMACSS led to a close match

in final conditions (with <8 per cent difference in both mass and half-mass radius) losing slightly more mass during its evolution, and reaching smaller final radii. For these three clusters the final radii are smaller, because the cluster did not expand as much as in the MOCCA simulation. For M4, the radius did expand up to 2.87 pc in the evolution with EMACSS, but near the end of the simulation the cluster already started to contract due to stellar evaporation. For NGC 6397, we have almost an exact match in final half-mass radius (<1 per cent difference), but the amount of mass-loss is less, leading to a difference of ∼21 per cent in linear mass with respect to the DS.

For G1, the cluster modelled with EMACSS more mass than the cluster modelled with a scaled *N*-body simulation (∼6 per cent difference in mass), but it also expanded more (∼25 per cent difference in radius). However, we note that in calculating the scaled-up version of the initial mass and half-mass radius of G1 found by Baumgardt et al. (2003b), we assumed that the same amount of mass-loss and stellar evolution induced expansion occurred as in the small-scale model. This does not have to be the case. Therefore, it could be that the scaled up initial condition from which we start evolving with EMACSS is different from the actual scaled up version of the initial condition of Baumgardt et al. (2003b), which would cause the differences in final mass and half-mass radius. For Pal 4 and Pal 14, we see that on average the direct *N*-body modelling caused the modelled clusters to lose slightly more mass than the clusters modelled with EMACSS leading to <15 per cent difference in mass for Pal 4 and <21 per cent difference in mass for Pal 14. For both Pal 14 and Pal 4, the EMACSS clusters expanded a bit more (<4 per cent and <2 per cent difference in radius, respectively).

For *ω* Cen, the EMACSS results compare less well to those obtained from MOCCA. Their simulated cluster lost substantially more mass (leading to an ∼59 per cent difference in linear mass). We could not compare the final half-mass radii, since Giersz & Heggie (2003) did not provide this, as described in Section 3.2.1. It could be that our assumption for calculating what the initial half-mass radius for the best fit of Giersz & Heggie (2003, see Section 3.2.1) was incorrect and that their initial half-mass radius was somewhat smaller or larger. Starting at a different initial radius could lead to a different amount of mass-loss. However, we have done several EMACSS runs for *ω* Cen, starting at the same initial mass, but with different initial half-mass radii in the range 0.01–30 pc and we saw that the amount of mass-loss changed only minimally. The mass-loss changed at most by a factor ∼1.08 between two radii in this range. For initial half-mass radii >20 pc the amount of mass-loss decreased. Only for clusters initially more compact than 0.5 pc will the amount mass-loss increase significantly, but not as much as in the MOCCA simulation. It is also not likely that *ω* Cen started out so compact, see Section 4.3. There is also poor agreement between EMACSS and the direct *N*-body results for the open cluster M67. Again, we see that the cluster simulated with EMACSS lost substantially less mass. Furthermore, the EMACSS cluster expanded by almost a factor 2 during its evolution, whereas the final half-mass radius of the cluster modelled with direct *N*-body integration is even slightly smaller than the initial one. These differences require some explanation.

Besides starting from the same initial total mass and half-mass radius, we kept the conditions of our simulation as similar as possible to those of the DSs. However, there are a number of parameters that could not be taken equal between the codes. One of these parameters is the initial number of stars. Since EMACSS is currently tested against *N*-body simulations for only one value of the initial mean mass $(\bar{m} = 0.64\,M_\odot)$ we always used this value for all our
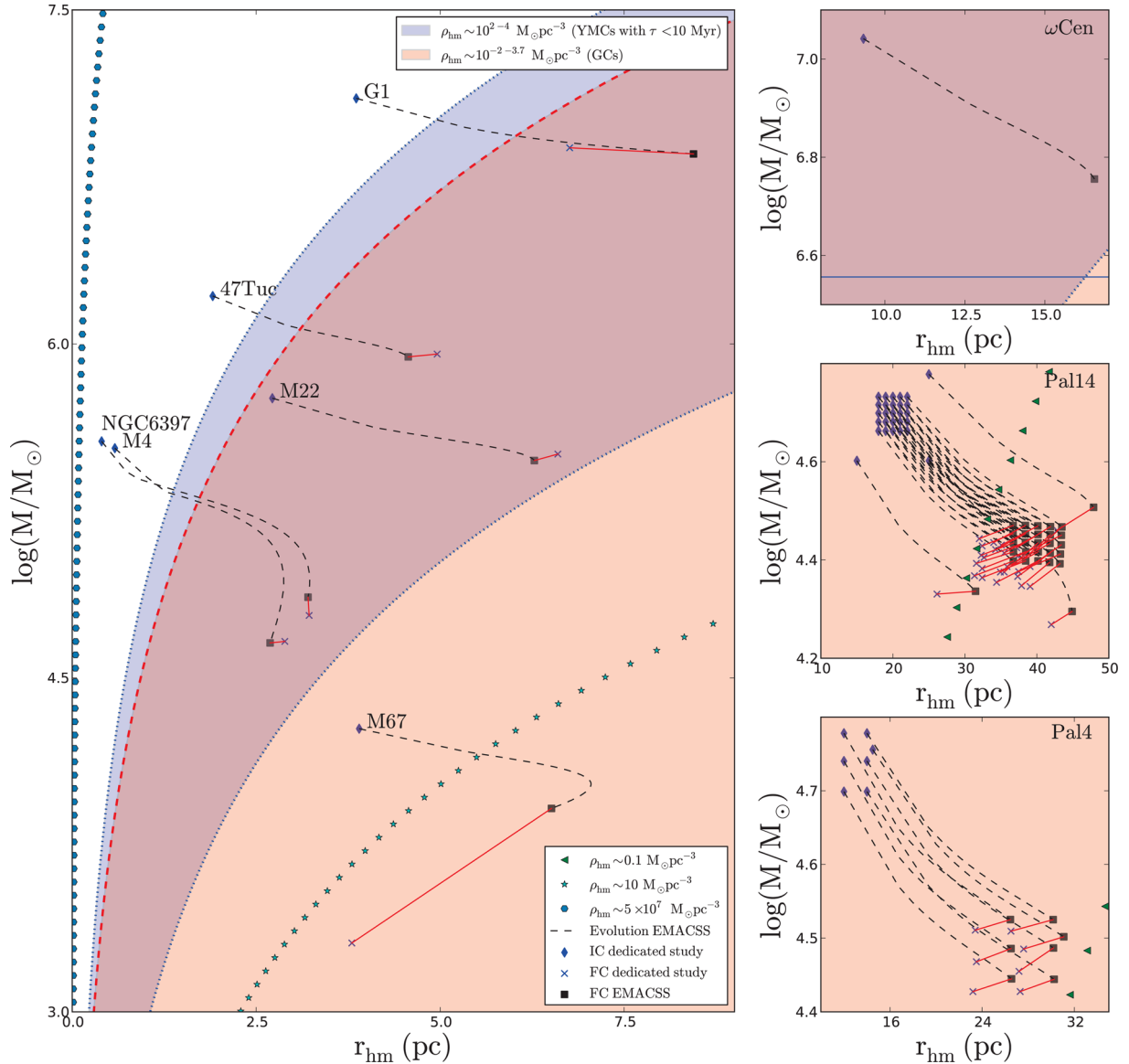
Figure 5. Direct comparison between EMACSS and the DSs by running EMACSS from the best-fitting initial condition of each DS. Each panel shows the total mass versus half-mass radius for one of the nine validation clusters. The blue diamond(s) and cross(es) show the best-fitting initial and final condition(s), respectively, of the DS; the black dashed line shows the evolution with EMACSS when started from the initial condition of the DS and the black square shows the final condition of this evolution with EMACSS. For ω Cen we show a blue line, indicating the final mass of the DS, since their final half-mass radius was not given. For Pal 4 and Pal 14, we compare to more than one model, so we connect the final conditions of the DS and EMACSS with a red solid line for clarity. As a comparison, we also plot the minimum densities a cluster needs to have in order to be stable against the tidal disruption of a galaxy ($\rho_{hm} \sim 0.1\,\mathrm{M}_\odot\,\mathrm{pc}^{-3}$ Bok 1934, green triangle line) and against passing giant molecular clouds ($\rho_{hm} \sim 10\,\mathrm{M}_\odot\,\mathrm{pc}^{-3}$ Spitzer 1958, cyan star line). The turquoise hexagon line shows a mean density of $\sim 5 \times 10^7\,\mathrm{M}_\odot\,\mathrm{pc}^{-3}$ that might be required for a cluster with a half-mass radius of 0.2 pc to form an IMBH via a runaway merger (McMillan 2008). We furthermore show the range of observed half-mass densities for globular clusters, $\rho_{hm} \sim 10^{-2-3.7}\,\mathrm{M}_\odot\,\mathrm{pc}^{-3}$, (red shaded region) and the range of present-day observed half-mass densities for clusters younger than 10 Myr ($\rho_{hm} \sim 10^{2-4}\,\mathrm{M}_\odot\,\mathrm{pc}^{-3}$ Portegies Zwart et al. 2010) (blue shaded region); the purple shaded region is the overlap of these blue and red regions.

simulations. This means that once we set the initial total mass of the cluster, we immediately set the initial total number of stars as well, which was different from the initial number of stars in each of the dedicated models, see Table 3. This lead to different initial half-mass relaxation time-scales, t_{rh}, with a larger t_{rh} for larger N. The initial half-mass relaxation time in the simulations of the DSs for M67, ω Cen, Pal 4 and Pal 14, respectively, was a factor 1.23, 1.47, 1.28 and 1.12, respectively, smaller than the EMACSS simulations. One would thus intuitively expect the clusters with shorter initial half-mass relaxation times to dissolve quicker, and this would lead

to a relatively quicker mass-loss in the first phase of its life (Lamers, Baumgardt & Gieles 2010). Furthermore, Heggie & Hut (2003) explain that in larger models, i.e. models with larger N, the escape rate per relaxation time is larger. This could explain why the DSs on M67, ω Cen, Pal 4 and Pal 14 lost more mass, since they start with a larger number of stars initially. For the clusters M4, M22 and 47 Tuc, the evolution with EMACSS started out with larger number of stars, and thus larger initial half-mass relaxation times by a factor 1.09, 1.07 and 1.25, respectively. Here, we thus see that the simulated clusters with EMACSS lost more mass, but not by much, see
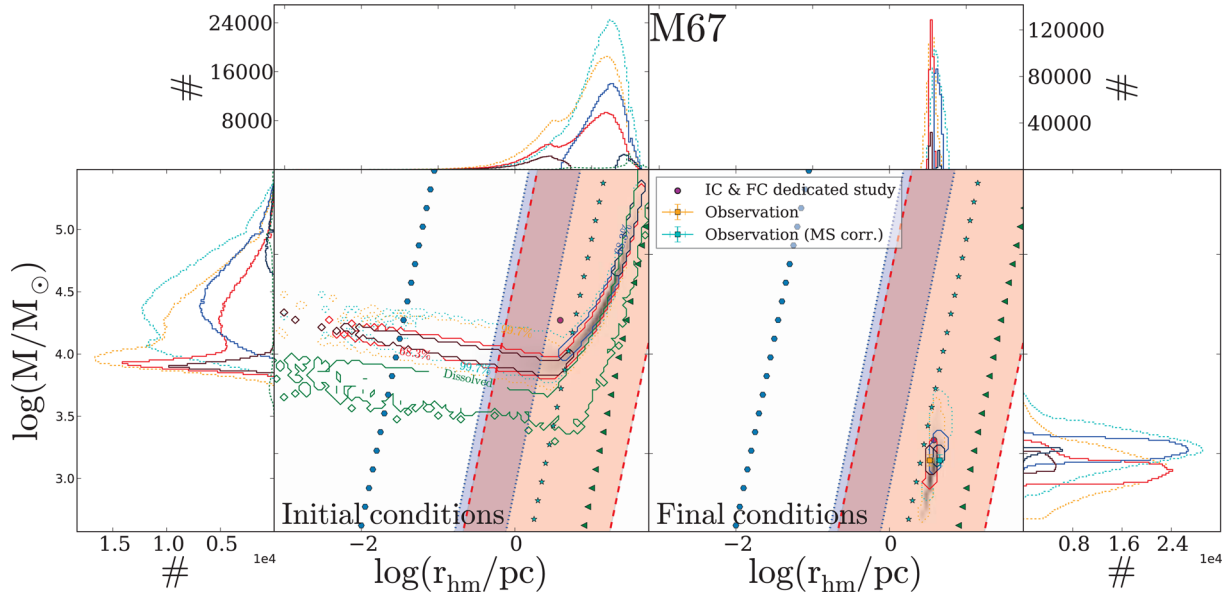
Figure 6. The same as in Fig. 2, but for the cluster M67 and with more details: the contours and histograms of the 99.7 per cent confidence level (dotted), the 68.3 per cent (solid) confidence level and the $p > 0.9p_{\max}$ (solid) initial conditions for both the simulations without (yellow, red and brown, respectively) and with (cyan, blue and dark blue, respectively) a correction for MS. The green contour and histograms show the clusters which dissolved before reaching the age of the cluster, τ_{obs}. The shaded regions, the lines depicted by green triangles, cyan stars and turquoise hexagons are as in Fig. 5.

Fig. 5. For NGC 6397 and G1, the initial number of stars of the DSs was not given.

Also, the prescription of stellar evolution and the (mass limits of the) IMF used by EMACSS and by the DSs and sometimes the galactic potential, setting the tidal field, were different. All this taken together led only to moderate differences in the final cluster total mass and half-mass radius for the clusters NGC 6397, M4, M22, Pal 4, 47 Tuc, Pal 14 and G1, but to more significant difference for ω Cen and M67. For M67, for example, it led to a larger initial Jacobi radius ($r_{\mathrm{J}} = 37.6$ pc) in EMACSS than the (similar) tidal radius ($r_{\mathrm{t}} = 31.8$ pc) in the N-body simulation.[7] This, in part, explains the smaller amount of mass-loss in the simulation with EMACSS and hence the overall larger amount of expansion. However, for ω Cen the difference in mass-loss cannot be explained by this, since we had an initial Jacobi radius similar to the tidal radius in the MOCCA simulation ($r_{\mathrm{J}} = 89.9$ pc; $r_{\mathrm{t}} = 90$ pc).

Another difference is that all DSs (except for Giersz & Heggie 2003) include some direct prescription for binaries, whereas the version of EMACSS used for this study does not. For each globular cluster in our sample, the DSs had only a small ($<$1 per cent) or no primordial binary fraction, so the effects that binaries have on the evolution of global cluster parameters such as total mass and half-mass radius are expected to be small here. Thus for validation purposes, binaries are not expected to cause major differences in the results between EMACSS and the DSs for this sample of globular clusters. For open cluster M67, however, a large initial binary fraction of 50 per cent was assumed in Hurley et al. (2005) and they showed that this fraction even increased throughout the 4 Gyr of evolution, also due to the evaporation of single stars. So for M67, we do expect binaries to play an important role in at least the cluster dynamics and this could certainly result in a very different evolution when compared to the evolution without binaries. This therefore also contributes to the difference between EMACSS and the direct N-body simulation

of M67. Just like mass-loss due to stellar evolution, hard binaries are expected to cause expansion of the half-mass radius (Giersz & Heggie 2011), and so based on this type of binaries alone one would not expect the cluster evolved with EMACSS to have expanded more. However, it is not obvious what to expect in terms of expansion of the half-mass radius for a steady 50 per cent fraction of primordial and dynamically formed, hard and soft binaries. An interesting side note is that when we continued the evolution for M67 for another $\sim$5 Gyr, it reaches a mass and half-mass radius within 4 per cent of those of Hurley et al. (2005). This might suggest that the presence of binaries accelerates the evolution. To test this hypothesis, we are running an N-body simulation similar to the one conducted by Hurley et al. (2005), but without binaries, of which we will show the results in forthcoming work.

The fact that EMACSS is designed for evolving globular clusters instead of open clusters is not in itself a reason for the sparse agreement. The majority of open clusters reside in the disc and they are more likely to undergo encounters with giant molecular clouds, which have dramatic effects on the cluster evolution (Gieles et al. 2006). However, even though EMACSS does not include these effects, neither did the simulations of Hurley et al. (2005), so for the comparison between the two codes for the validation, this should not matter. Applying our method to an open cluster for actually constraining its initial conditions, this will become important and some prescription taking into account these disruptive events is required.

4.3 Independent EMACSS-MCMC runs

The results of the independent EMACSS-MCMC runs in 2D are shown in Figs 6–14 and are summarized in Table 3, where we compare the observations and EMACSS' best-fitting results for the simulations where we did not correct the observations for MS (see Section 2.3) and EMACSS' best-fitting results for the simulations where we did correct for MS, in row one, four and five, respectively, per cluster. We see that for some clusters (M67, NGC 6397, M4, M22 and

---

[7] Note again that $r_{\mathrm{J}} = r_{\mathrm{t}}$ for the type of potential we use here.
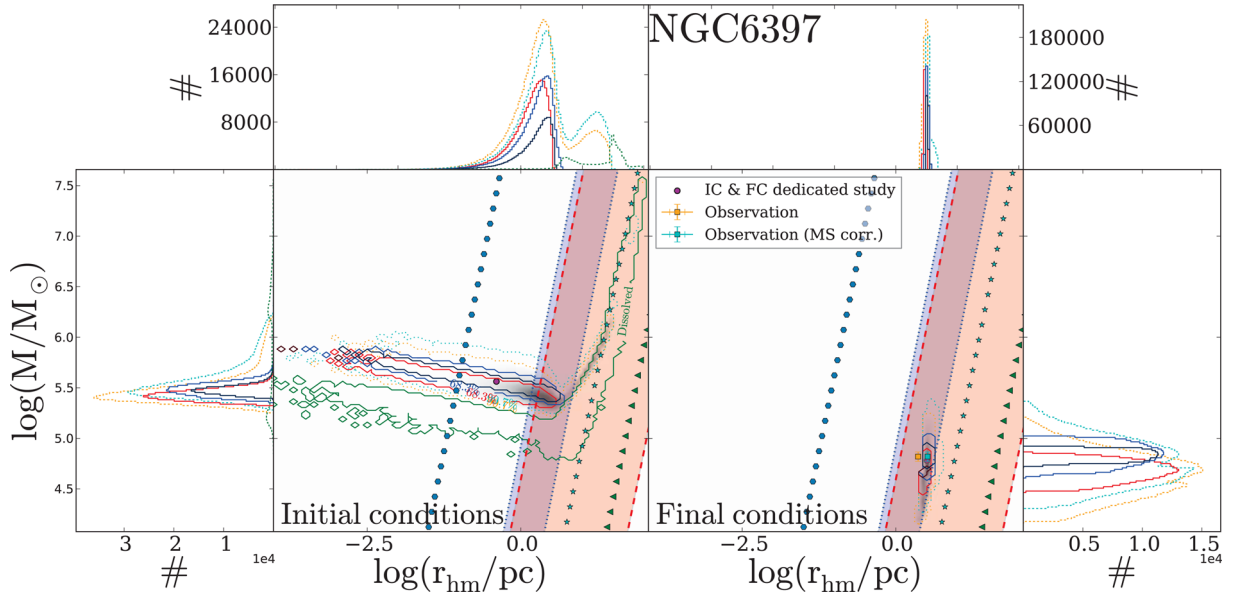
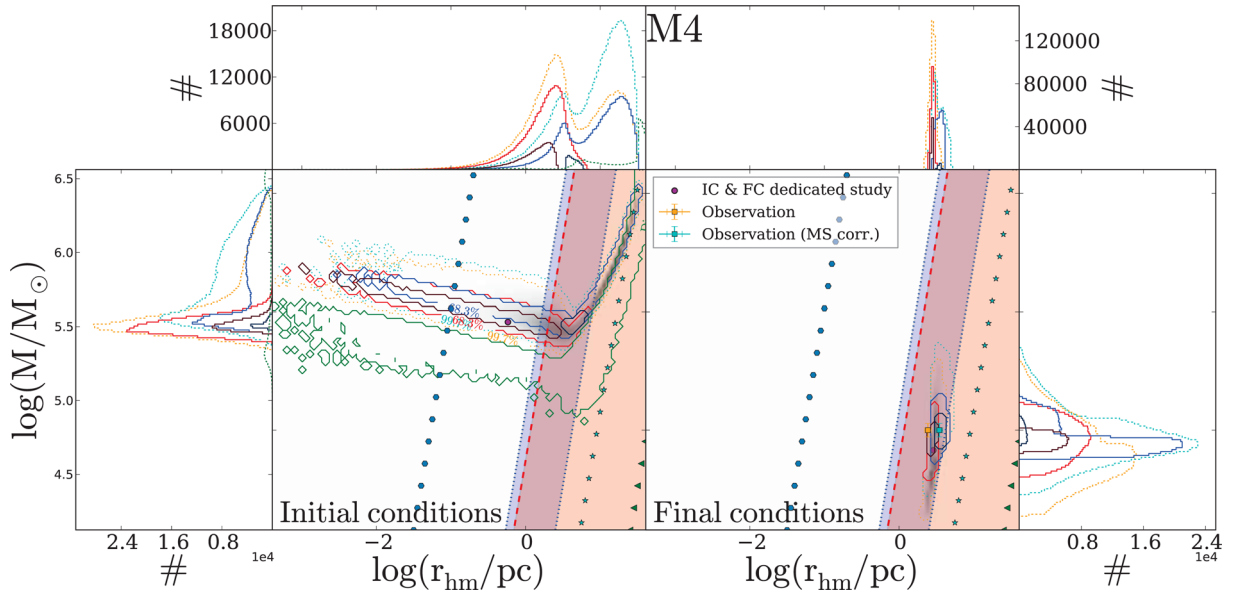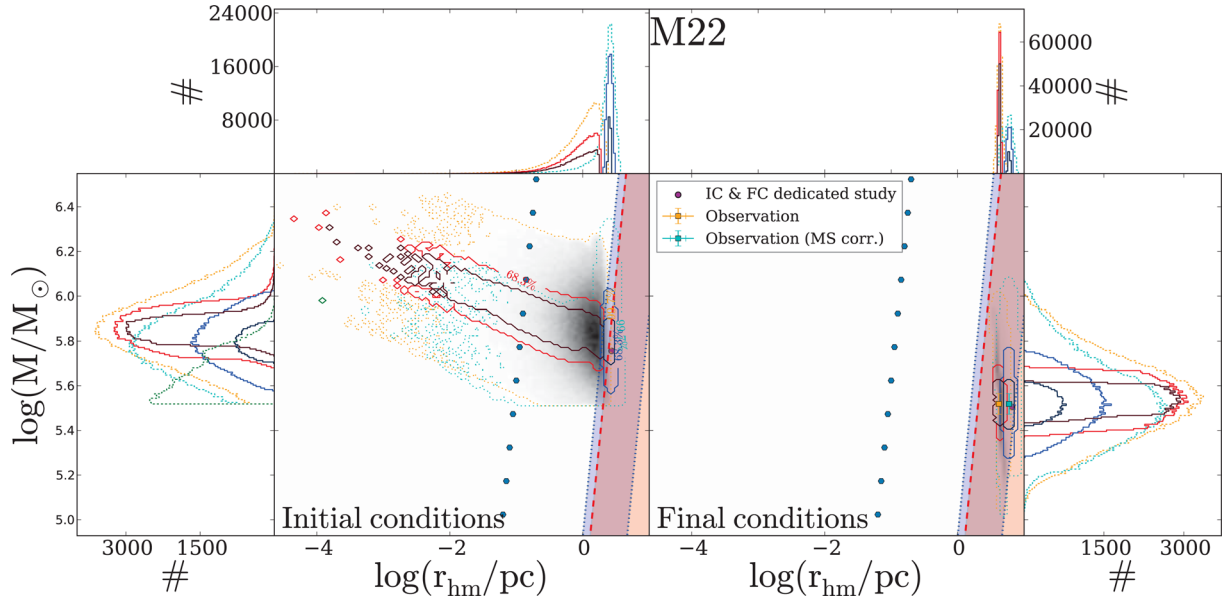**Figure 7.** The same as Fig. 6, but for the cluster NGC6397.

Figure 8. The same as Fig. 6, but for the cluster M4. The results in this figure are as in Fig. 2.

47 Tuc), the initial conditions extend to small half-mass radii and high initial half-mass densities. These initial conditions correspond to an average distance between the cluster stars on the order of 10 au, and thus these densities are too high to be physical. In Figs 6–14, we show the range of observed half-mass densities for globular clusters, $\rho_{hm} \sim 10^{-2-3.7}\,\mathrm{M_\odot\,pc^{-3}}$, calculated according to

$$\rho_{hm} = 3M/(8\pi r_{hm}^3), \qquad (10)$$

see also fig. 1 of Portegies Zwart et al. (2010), using the 'half-mass radii' of Harris (2010) corrected for MS (see Section 2.3) and masses calculated by using the mass-to-light ratios, M/L, from McLaughlin & van der Marel (2005) – or a constant M/L ~ 1.45 (McLaughlin 2000) for clusters which do not have an observational value – and the absolute V-band magnitudes of Harris (2010, red shaded region). The high-ρ_{hm} initial conditions mentioned above are significantly larger than the ones observed today and this is

attributable to the small initial half-mass radius the MCMC sampled for these clusters. One could argue that the current half-mass densities need not be representative for the initial half-mass densities, and (globular) clusters may have had larger initial half-mass densities at younger ages. However, from Figs 6–9 we can see that the range of present-day observed half-mass densities for clusters younger than 10 Myr is still a few orders of magnitudes less dense than the initial densities for M67, NGC 6397, M4 and M22 in our calculations. One could also argue that the precursors of the old (globular) clusters might have been very different from the young clusters today. High densities might even be essential to enable run-away mergers as a pathway to produce intermediate black holes (IMBHs) in globular clusters (McMillan 2008). McMillan (2008) gives the example that a mean density of $\sim 5 \times 10^7\,\mathrm{M_\odot\,pc^{-3}}$ would be required for a cluster with a half-mass radius of 0.2 pc. Moreover, Pfalzner et al. (2014) ran semi-analytical models for the formation

Figure 9. The same as Fig. 6, but for the cluster M22.
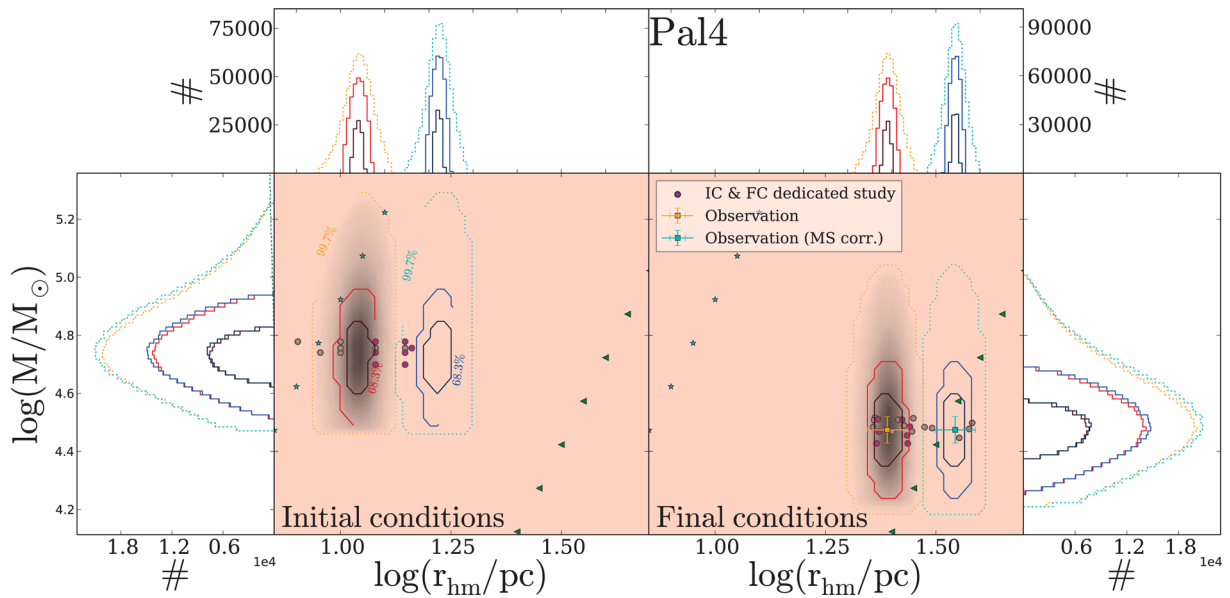
Figure 10. The same as Fig. 6, but for the cluster Pal4.

of star clusters and show that the central cluster area can have stellar densities of $\sim 4 \times 10^5 \, \mathrm{M_\odot \, pc^{-3}}$ at the moment of gas expulsion; see fig. 2 of Pfalzner et al. (2014). However, densities greater than $\sim 10^{10} \, \mathrm{M_\odot \, pc^{-3}}$ seem too extreme. Moreover, it is important to keep in mind that the initial conditions we derive in this work are the conditions of a star cluster after residual gas expulsion and re-virialization. Since all star clusters expand due to residual gas expulsion (Baumgardt & Kroupa 2007), the clusters are expected to be even denser, i.e. more massive and more compact, directly after cluster formation.

The reason the MCMC code selected these initial conditions is that we have not build in a criterium for only selecting initial conditions below a maximum allowed initial half-mass density, simply because we do not know what this upper limit should be. We also considered it to be better not to limit the MCMC code, but to include

possible density limits only in the analysis phase. Furthermore, for the four clusters (M67, NGC 6397, M4 and M22) where probable initial conditions are found in the high half-mass density regions of parameter space, we see that the probable initial conditions are degenerate (see Section 4.3.3). From the brown contours in Figs 6–9, we can conclude that lower density initial conditions are practically equally probable.

The results of the 5D simulations are shown in Fig. 15 and in the figures in the Appendix A. Table 4 furthermore shows the characteristics of our best-fitting model without a correction for MS. From the brown contours in Fig. 15, we can once again see that the most probable 0.1 per cent of the initial conditions are found in the most sampled region, but that a probable initial condition does not have to have each parameter to originate from the most sampled region.
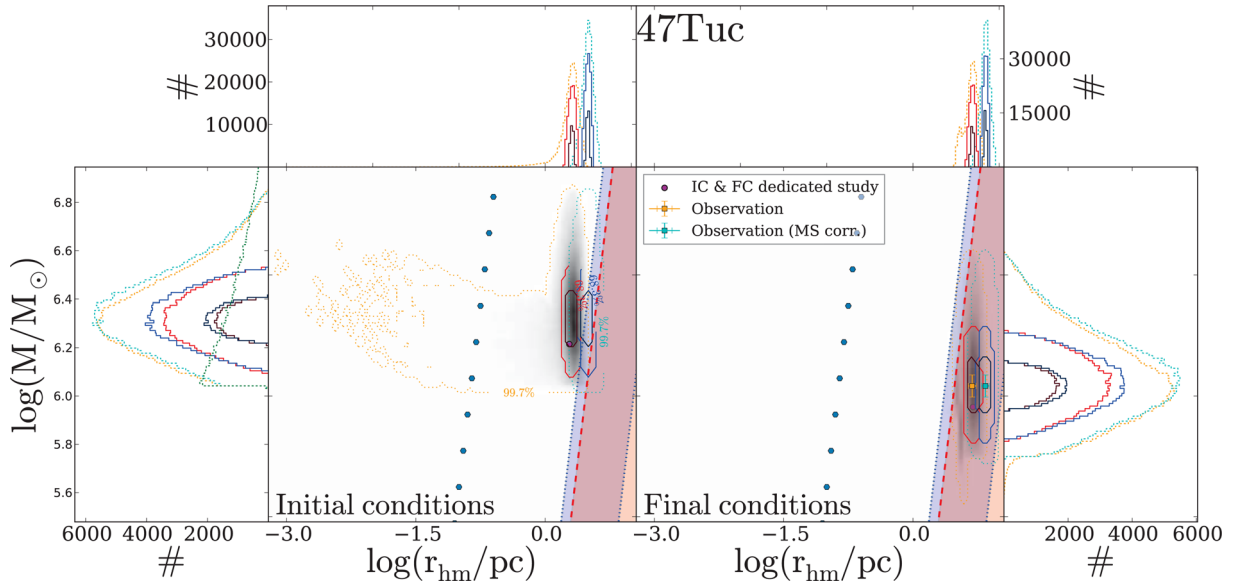
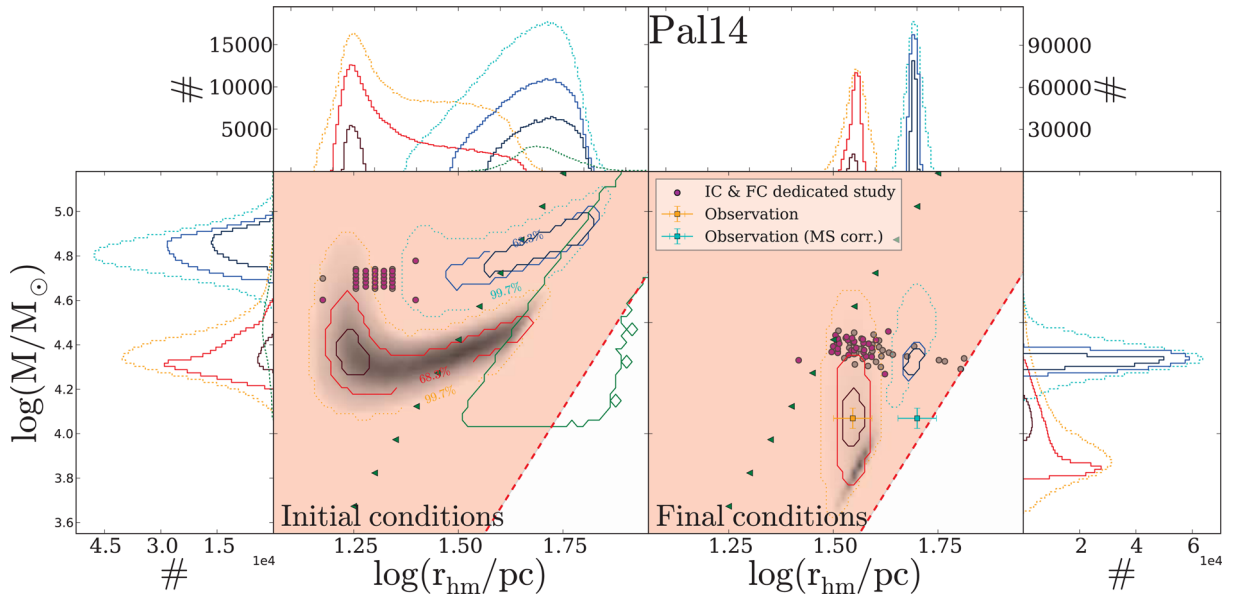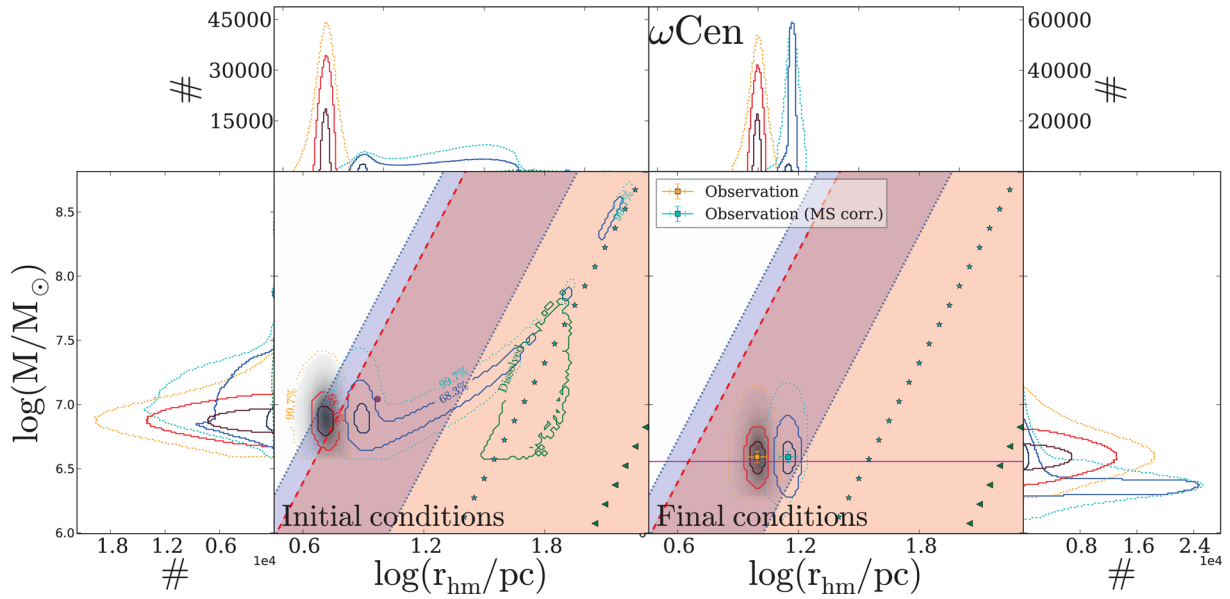**Figure 11.** The same as Fig. 6, but for the cluster 47Tuc.

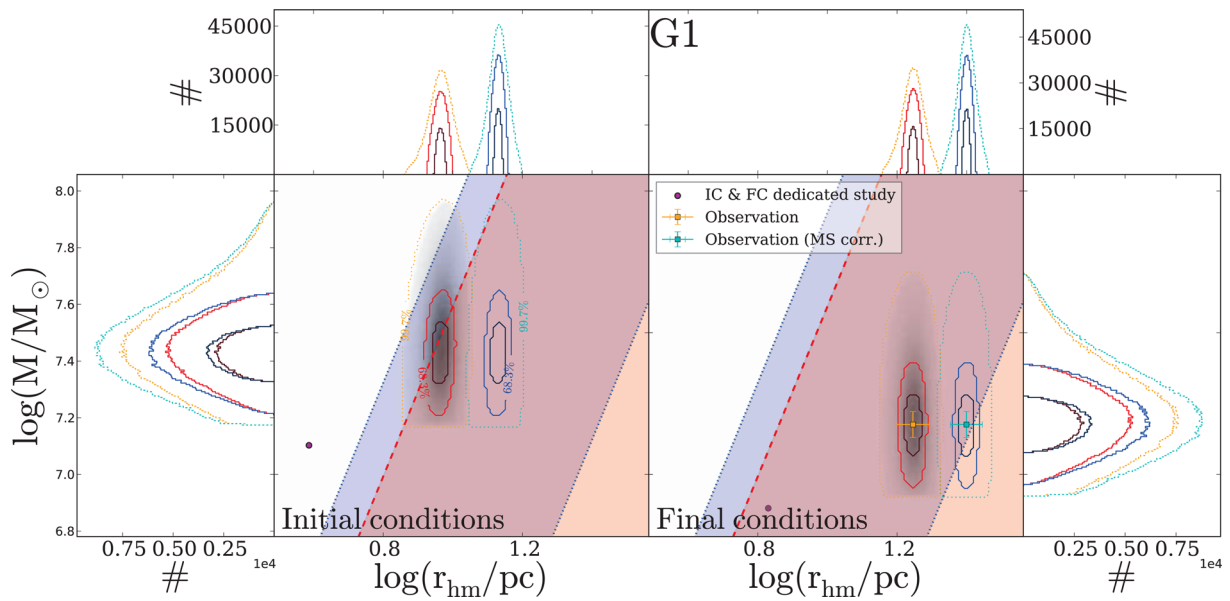**Figure 12.** The same as Fig. 6, but for the cluster Pal14.

4.3.1 Correcting observations for MS

The DSs to which we compare our results did not correct their observations for MS. This is because it is difficult to determine the amount of MS that the cluster experienced and hence the ratio r_{hm}/r_{phl} at $t = \tau_{obs}$, i.e. the factor c_{MS} in Section 2.3. However, many globular clusters show signs of MS. Even the outer halo cluster Pal 14 has recently been shown to be (primordially) mass segregated (Frank, Grebel & Kuepper 2014). For this reason, we investigated what the influence of observing a mass segregated cluster, but not correcting the half-mass radius for it, could have on the determined initial conditions of the cluster. We did this for a fixed ratio r_{hm}/r_{phl}, see Section 2.3, but the outcome will illustrate the importance of correcting for MS on the interpretation of the evolution of the observed cluster.

The first thing we can see from Figs 6–14 is that correcting the observations for MS or not, affects the shape and location of the corresponding 99.7 per cent confidence region in the initial conditions. In other words, it changes which initial conditions are considered probable. In some cases these changes are mild, such that the 99.7 per cent confidence regions still show some overlap, e.g. for M67, NGC 6397, M4, M22; in Section 4.3.3 we will see that this has to do with the degeneracy due to core-collapse. But in the other cases, the shapes or location of the 99.7 per cent confidence regions are different. And in almost all cases, the contours of highest probability are completely separated. It even turns out that the factor $c_{MS} = 1.9$ we used for the globular clusters (Hurley 2007) is typical for clusters of low density, whereas this factor seems to increase for more dense clusters (Mirek Giersz, private communication). For denser clusters, we thus expect the differences in the

Figure 13. The same as Fig. 6, but for the cluster ω Cen.


Figure 14. The same as Fig. 6, but for the cluster G1.

initial conditions for the corrected and non-corrected simulations to be even more distinct. However, many studies do not aim to (just) fit structural parameters such as half-mass radius and total cluster mass, but aim to (also) have a good fit in the surface brightness profile, velocity dispersion profile and luminosity profile at multiple radii (Giersz & Heggie 2003; Baumgardt et al. 2003b; Hurley et al. 2005; Heggie & Giersz 2008; Giersz & Heggie 2009, 2011; Heggie & Giersz 2014); see Section 4.4. It will therefore be interesting to investigate whether a cluster that will be modelled with *N*-body or Monte Carlo simulations starting from one of the best-fitting initial conditions with a correction for MS, can produce the three above-mentioned profiles that match the observed ones equally well as a cluster starting at the best-fitting initial conditions without this correction.

For further validation purposes, we focus on the comparison between our simulations without a correction for MS to the results of the dedicated studies.

4.3.2 Dissolving clusters

From the Figs 6–14, we see that for each of the nine validation clusters, the modelled clusters which do not survive up to the cluster age are in most cases relatively larger (and sparser) and/or less massive than the clusters which do survive. Sometimes these clusters dissolved too sparse initial conditions were chosen by the MCMC code, which led to immediate (within a few Myr) dissolution. E.g. this is the case for all dissolving clusters for Pal 14, which have $\rho_{hm} > 0.1 \, M_\odot \, pc^{-3}$. In other cases, these clusters underwent
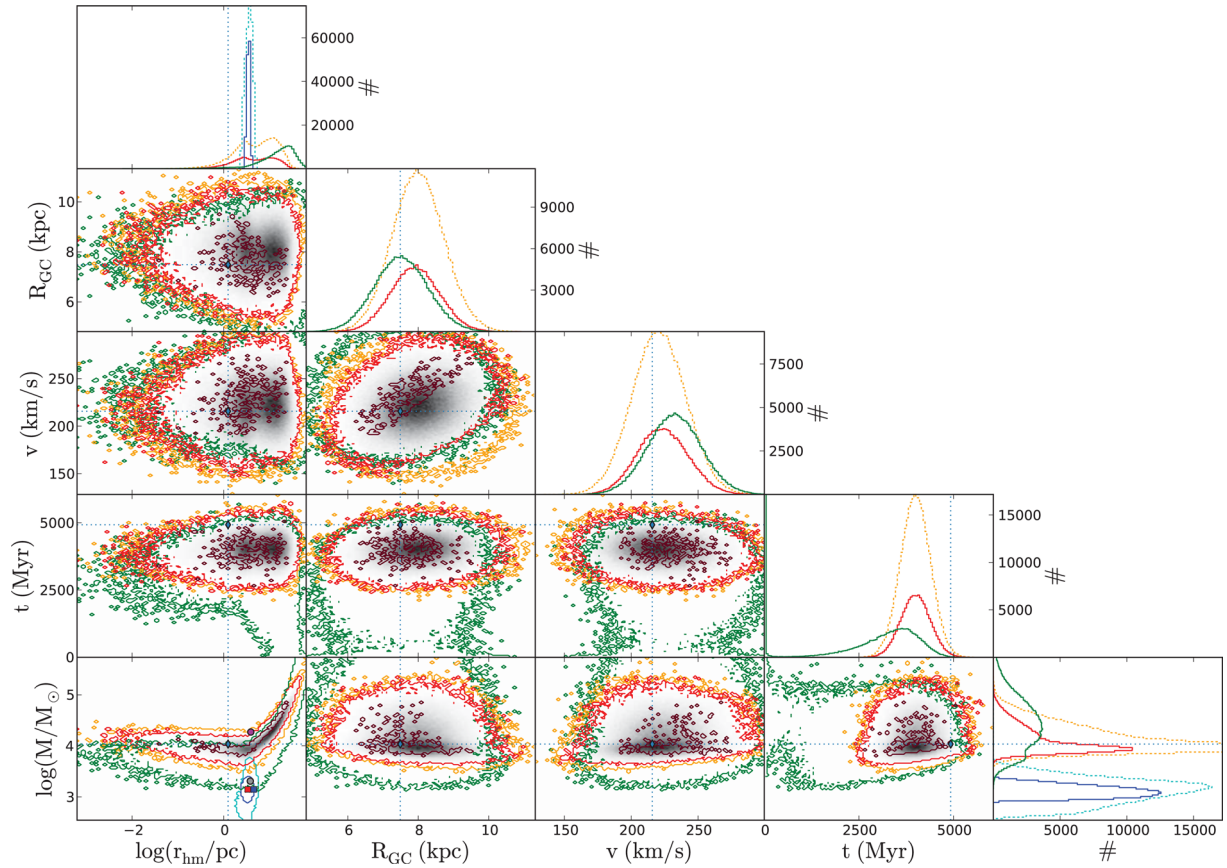
Figure 15. Initial (and final) condition distributions for cluster M67 from the 5D MCMC simulations with fitting parameters mass and half-mass radius, and nuisance parameters Galactocentric radius, orbital velocity and age, each with 10 per cent errors for the simulations which fit the observables without a correction for MS. Numbered from top to bottom, from left to right, in panels 2, 4, 5, 7, 8, 9, 11, 12, 13 and 14 show two-dimensional histograms in a black–white density plot of two of the five parameters initial mass, initial half-mass radius, initial Galactocentric radius, initial orbital velocity and (final) age against one another: the darker the area, the more initial conditions in this area were sampled. Overplotted on these two-dimensional histograms are the outer contours of the 99.7 per cent (yellow) and 68.3 per cent (red) confidence contours for the simulation fitted to observations without a correction for MS. The cyan and blue contour in panel 11 show the 99.7 and 68.3 per cent confidence contours of the final conditions in total mass versus half-mass radius, respectively. The brown contours show the most probable region with $p > 0.999 p_{max}$. The green contours show the clusters which dissolve before reaching the age of the cluster, τ_{obs}. The red square with error bars show the observation of the cluster's current mass and half-mass radius when no correction for MS is made, and the blue square with error bars shows the observable with a correction. The pink filled circle denotes the initial condition used by the DS, which evolves to the final condition shown by the grey filled circle in the right-hand panel. The corresponding projected histograms are shown in panels one, three, six, 10 and 15.

Table 4. Best-fitting parameters for the 5D simulations fitting the observations without a correction for MS. For each validation cluster mentioned in the first column nine parameters of the best-fitting model given. The parameters are the initial number of stars N_i in column two, the initial mass M_i (in 10^5 M$_\odot$) in column three, the initial half-mass radius $r_{hm,\,i}$ (in pc) in column four, the galactocentric radius R_{GC} (in kpc) in column five, the orbital velocity v (in km s^{-1}) in column six, the final number of stars N_f in column seven, the final mass M_f (in 10^4 M$_\odot$) in column eight, the final half-mass radius $r_{hm,\,f}$ (in pc) in column nine and the age t of the cluster (in Gyr) in column 10.

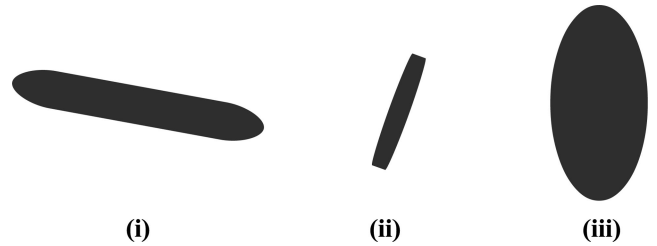| Cluster	N_i	M_i (10^5 M$_\odot$)	$r_{hm,\,i}$ (pc)	R_{RG} kpc	v km s^{-1}	N_f	M_f (10^4 M$_\odot$)	$r_{hm,\,f}$ (pc)	t Gyr
M67	17.0 k	0.108	1.24	7.49	216	2.18 k	0.139 k	3.35	4.93
NGC 6397	579 k	3.70	1.52	1.51	265	99.5 k	6.37	2.37	9.89
M4	820 k	5.25	0.179	1.45	244	98.3 k	6.29	2.45	11.5
M22	988 k	6.32	1.65	4.59	197	516 k	33.0	4.17	10.8
Pal 4	83.4 k	0.534	11.1	96.6	219	46.6 k	2.98	24.5	10.6
47 Tuc	3.21 M	20.5	1.97	3.57	219	1.72 M	110	4.87	13.8
Pal 14	34.8 k	0.222	16.8	88.3	236	18.3 k	1.17	35.2	12.1
ω Cen	11.7 M	74.9	5.12	1.23	218	6.09 M	390	8.89	12.4
G1	41.2 M	264	9.38	42.8	234	23.4 M	1501	17.6	10.3

Figure 16. The distinction between the initial conditions (top panel) and final conditions (bottom panel) of the model clusters which undergo a core-collapse during their evolution (red) and those which do not (blue) for the 2D run for the cluster M4 without a correction for MS.

Figure 17. A schematic overview of the three morphologies: (i) a roughly horizontal distribution with a negative slope towards small half-mass radii; (ii) a distribution with a positive slope reaching to large radii; (iii) a two-dimensional Gaussian-shaped distribution at relatively larger initial half-mass radii than the previous case.

the model clusters which undergo a core-collapse during their evolution (red) and those which do not (blue) for the 2D run for the cluster M4 without a correction for MS. We can see that the clusters which undergo a core-collapse in our simulations generally start out with smaller half-mass relaxation times, $log(t_{rh}) \lesssim 2.8$ in this example for M4; these clusters also have relatively small radii. For those clusters with $log(t_{rh}) \gtrsim 2.8$, we see that for a fixed radius the clusters that did not yet undergo a core-collapse are more massive. This is what one would expect from the fact that the core-collapse time, t_{cc}, scales with the half-mass relaxation time, t_{rh}, which increases for large r_{hm} and large N. The lower mass clusters with $log(t_{rh}) \gtrsim 2.8$ also form a degeneracy towards larger radii and masses. With EMACSS we keep track of the evolution of the derivative of the half-mass radius, dr_{hm}/dt. It turns out that the degeneracy towards large radii is produced by the fact that those clusters experienced a phase of contraction. This is consistent with the fact that once clusters have reached a certain relatively large radius (due to expansion), the escape of stars over the Jacobi radius becomes dominant (Gieles & Baumgardt 2008). The large amount of mass-loss of these clusters corresponds to the decrease of their half-mass relaxation time, such that they will still undergo a core-collapse. This degeneracy is limited on the low-density side by the dissolution region.

When we examine Figs 6–14, we notice that the 99.7 per cent confidence regions in the initial conditions are built-up out of three characteristic shapes (see also Fig. 17:

(i) a roughly horizontal distribution with a negative slope towards small half-mass radii. This distribution has high posterior probabilities for a large spread in half-mass radii and a moderate spread in mass. The 99.7 per cent confidence regions of the clusters M67, NGC 6397, M4 and M22 have this morphology for both our models with and without a correction for MS. This distribution corresponds to the clusters that undergo a core-collapse within their evolution time, τ_{obs}.

(ii) A distribution with a positive slope reaching to large radii. This characteristic shape is seen in the initial conditions for the clusters M67, NGC 6397, M4 and Pal 14 for the models with and without a correction for MS and for ω Cen for the models with a correction for MS. This distribution corresponds to the clusters that experienced a phase of contraction.

(iii) A two-dimensional Gaussian-shaped distribution at relatively larger initial half-mass radii than the previous case. The 99.7 per cent confidence regions of the clusters Pal 4 and G1 have purely this morphology for the models with and without a correction for MS. This shape is also seen in the 99.7 per cent confidence regions of the clusters M22, 47 Tuc, Pal 14 and ω Cen for the

relatively quick mass-loss, dissolving before reaching the observed cluster's age. The surviving and dissolving initial conditions are well separated, except at the borders of the two distributions, which is to be expected. From Fig. 15, we see that for the 5D runs the dissolution regions projected on to a two-dimensional plane are not well separated from the surviving (high posterior probability) regions anymore. See e.g. panel 11 of Fig. 15, where the 99.7 per cent confidence contour largely overlaps with the dissociation region contour. The reason for this overlap is simply because that figure is a projection of a five-dimensional space of initial conditions on to a two-dimensional space. In other words, a suitable initial condition $(r_{hm, i}, M_i)$ for one combination of the nuisance parameters (R_{GC}, v, τ), could be dissolving for another combination of these nuisance parameters. If we were to take 2D projections of this five-dimensional space at distinct combinations of (R_{GC}, v, τ), the dissociation regions should again be well separated from the surviving regions, except at borders where we expect to have an overlap again.

4.3.3 Degeneracies: dynamical age and morphology

We can divide the surviving clusters in two types of clusters: (1) the clusters which underwent a core-collapse and are now in the third and 'balanced' phase of their evolution and (2) the clusters which did not undergo a core-collapse (yet) and are still in the second and 'unbalanced' phase of their evolution (see Section 2.1 for a definition of these evolutionary phases). See e.g. Fig. 16 where we make a distinction between the initial and final conditions of

models with and without a correction for MS. The initial conditions from this distribution correspond to clusters that do not undergo a core-collapse within the evolution time. In this case, the initial conditions are better constrained.

We see the morphology of 99.7 per cent confidence regions are built-up out of one or more of the three shapes above. The 99.7 per cent confidence regions of the clusters M67, NGC 6397 and M4 are built-up out of morphology (i) and (ii) for models with and without a correction for MS. The 99.7 per cent confidence regions of the clusters M22 for both MS-corrected and not MS-corrected models and 47 Tuc for the not MS-corrected models have a morphology consisting of shapes (i) and (iii), which shows that both core-collapsed and not core-collapsed clusters could fit the observed mass and half-mass radius. The 99.7 per cent confidence region of the clusters Pal 14 for both MS-corrected and not MS-corrected models and ω Cen for models with a correction for MS consist of morphological shapes (ii) and (iii).

From the morphologies (i) and (iii) in Figs 6–14, we see that the morphology roughly changes along the sequence (i) → (i) & (iii) → (iii). Since the clusters are mentioned in the order of increasing current half-mass relaxation time, which is a proxy for the dynamical age of a star cluster, we thus see a connection between the morphology of probable initial conditions and the dynamical age of a cluster. The connection is quite intuitive. First, the morphology is connected to the core-collapse state of the cluster [(i) core-collapsed; (iii) not core-collapsed]. When a cluster undergoes core-collapse, the half-mass radius increases, because energy is injected into the halo (Lynden-Bell & Eggleton 1980; Baumgardt, Hut & Heggie 2002). The amount by which the half-mass radius increases depends on many different cluster characteristics, such as the binary fraction, as well as on the interactions taking place. Two clusters with the same initial conditions, but with a different initial distribution of positions and velocities of the stars, will have different pathways to core-collapse and the halt thereof, also known as statistical fluctuations (Giersz & Heggie 2009). It is therefore practically impossible to sharply constrain the initial half-mass radius of the cluster, because we do not know the amount by which it increased during core-collapse. So there are many different possible initial half-mass radii and hence we see a degeneracy in the initial distribution of half-mass radii. When on the other hand the cluster has not yet undergone core collapse, there is only a narrow range of possible initial half-mass radii and thus the initial half-mass radii are better constrained.

Secondly, when the half-mass relaxation time is small, so is the core-collapse time, since $t_{\rm cc} \propto t_{\rm hm}$. So an observed cluster with low $t_{\rm hm}$ is more likely to have undergone a core-collapse and hence its initial condition distribution will have morphology (i). If an observed cluster has a higher $t_{\rm hm}$, there is a probability that the cluster comes from an initial condition which will undergo core-collapse during its evolution up to the observed clusters age, but also probability that the cluster comes from an initial condition which will not. This cluster will thus have an initial condition distribution made up of morphology (i) and (iii). The clusters with the largest half-mass relaxation times will not have initial conditions distributions with morphology (i), but rather (iii).

Morphology (ii) is associated with the contraction of the cluster, or, in other words, a decrease of the $r_{\rm hm}$. And just like with the degeneracy associated with core-collapse, it is practically impossible to constrain the half-mass radius sharply, because we do not know by which amount the cluster contracted. So many different evolutionary paths, each with different amounts of contrac-

tion, could have produced the current observables and therefore we have this degeneracy. To test our hypotheses for the connection between morphology of the initial condition distribution and the dynamical age of the cluster, we need to apply our method on a larger sample of clusters, which we are doing in forthcoming work. If the connection between the morphology and the dynamical age is indeed robust, then the initial conditions provided by our method gives an independent hint on to the core-collapse state of a cluster.

We will now compare our findings to the observations. For M67, we find that our best-fitting model without a correction for MS underwent a core-collapse. To the best of our knowledge, M67 is not classified as a post-core-collapse cluster and neither have we come across any other claims of open clusters going through core-collapse. However, Hurley et al. (2005) do mention that for binary-rich clusters there is no clear core-collapse, at least not in the way that is witnessed in simulations without primordial binaries, where high core densities need to be reached in order to form binaries (see e.g. Hurley et al. 2004). The fact that we find a post-core-collapse best-fitting cluster for M67, is most likely a direct result of not directly taking into account binaries within EMACSS, because it is the high binary fraction which causes open clusters to not undergo a core-collapse in a way that is found for globulars (Hurley et al. 2005).

Trager et al. (1995) classified ω Cen, M4, 47 Tuc and M22 as King profile clusters: these clusters were interpreted as clusters which have not undergone core-collapse yet. NCG 6397 was classified as a post-core-collapse cluster. Defining the term *dynamically old (young)* for clusters with a large (small) age over half-mass relaxation time ratio, $\tau_{\rm obs}/t_{\rm rh}$, the cluster NGC 6397 is dynamically old given its current half-mass relaxation time of 0.4 Gyr (Harris 2010), see also Table 2. Dynamically old clusters are more likely to have already undergone core-collapse, which is consistent with the classification. 47 Tuc and ω Cen are dynamically young given their current half-mass relaxation times of 3.55 and 12.3 Gyr, respectively (Harris 2010), and are thus both far from core-collapse (Trager et al. 1995). However, for M22 and M4 Harris (2010) lists relatively short half-mass relaxation times, 1.7 and 0.85 Gyr, respectively, such that these clusters have undergone a number of relaxation times. Moreover, Heggie & Giersz (2008) for the first time claimed that M4 is a post-core-collapse cluster, based on the observed behaviour of the core radius, $r_{\rm c}$, of their model of M4 (see their Fig. 5). Therefore, it is interesting to see that our best-fitting models without a correction for MS for both M4 and M22 have also undergone a core-collapse, and, as expected, the best-fitting model for ω Cen did not. 47 Tuc is an interesting case, because we find that there are initial conditions of model clusters within the 97 per cent confidence region which underwent a core-collapse, and initial conditions of model clusters which did not, see Section 4.3.3. However, our models show a favour for the not core-collapsed solutions, consistent with the observations (Trager et al. 1995).

Both Palomar 4 and 14 are classified as King profile clusters, so they are interpreted as clusters which have not yet reached the post-core-collapse phase (Trager et al. 1995). This is to be expected for dynamically young clusters with their current half-mass relaxation times, $t_{\rm rh}$, of 2.63 and 10.47 Gyr, respectively (Harris 2010). Our simulations also show that our best-fitting models had not undergone core-collapse yet. And also for G1, we find that the best-fitting conditions do not undergo core-collapse within its evolution up to its observed age. As argued in Section 4.4, given G1's half-mass relaxation time, it is reasonable to assume that G1 has not undergone core-collapse yet (Baumgardt et al. 2003b).
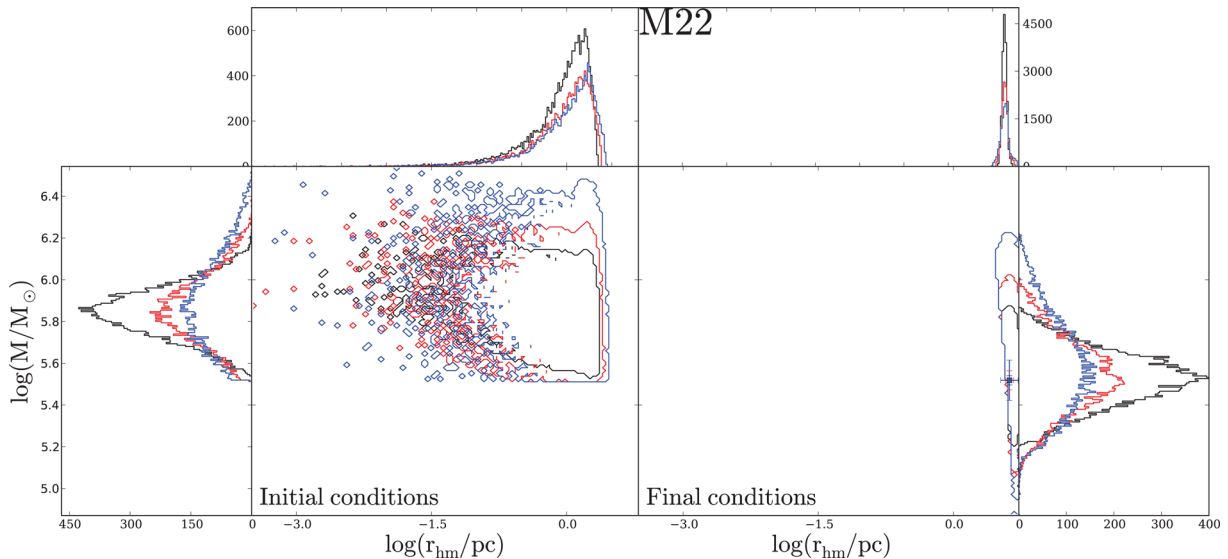
Figure 18. This figure is similar to the lower panels of Fig. 9, but this time we show the 99.7 per cent confidence contours for the simulation fitted to observations without a correction for MS, using a 5 per cent (black), 10 per cent (red) and 20 per cent (blue) error on the observables.

4.3.4 Accuracies on observables

In Fig. 18, we study how including smaller and/or larger errors on the observed mass and half-mass radius will effect the determined initial conditions. The figure shows the initial and final condition distributions in half-mass radius versus total mass for the cluster M22 for three different error percentages. We chose M22 for its characteristic initial condition morphology consisting of shapes (i) and (iii) and we wanted to see if this morphology is conserved if the observables had larger or smaller errors. Decreasing/increasing the errors also decreases/increases the size of the 99.7 per cent confidence region, but the degeneracy in the initial half-mass radius and the overall morphology remain the same. This makes it more likely that the result that M22 could both be a core-collapsed cluster and not core-collapsed cluster is robust and that it is not a consequence of not being able to distinguish between the two due to observational errors. We furthermore see that the lower the observational errors in the parameters mass and half-mass radius, the better one can especially constrain the initial mass of that cluster, but also slightly the half-mass radius.

In Fig. 19, we compare our 2D simulations with our 5D simulations to infer the stability of the probable initial conditions against observational errors in the galactocentric radius, orbital velocity and age – in essence combining the results from figures like Figs 6 and 15 per cluster. We can see that including distance, age and orbital velocity as nuisance parameters broadens the 99.7 per cent confidence regions for each of the clusters, and that this broadening is most visible for the clusters with a degeneracy [morphologies (i) or (ii)] in the high probability part of their initial conditions. This is because these clusters undergo either expansion or contraction and especially these processes are sensitive to the parameters setting the tidal field (R_{GC} and v) and the time that it could have expanded/contracted (τ). The morphology is conserved for all but one cluster; in these cases the 99.7 per cent regions are just broadened upwards and downwards. Upward if the variation in one of the nuisance parameters increases the strength of the tidal field (smaller R_{GC} and larger v); in these cases, the clusters must have started out more massive to withstand the larger amount of mass-loss. An upward shift can also be caused if the sampled age is larger than

τ_{obs}. This is because the cluster spends a longer time losing mass and thus must have started out with a higher mass to reproduce the same observed mass. In the opposite cases (decreasing the tidal field strength or smaller ages), we see a downward shift. See especially the clusters M67, NGC 6397, M4, Pal 14 and 47 Tuc in Fig. 19. M22 also has a degeneracy towards small initial half-mass radii, but the effects mentioned above are much weaker here. This could be due to the lower sampling of initial radii log (r_{hm}/pc) < 0.0.

We also observe a less prominent, but still visible shift in the initial conditions of the degeneracy-free clusters Pal 4 and G1 in Fig. 19. There we see that a stronger tidal field, respectively, a shorter evolution time, causes the initial conditions distribution to shift to slightly larger half-mass radii, indicating that slightly larger clusters are more probable to reproduce the observables in these cases. For the cluster ω Cen this shift due to the increase of tidal field strength even goes that far, that the morphology changes: (iii) → (ii) & (iii). This indicates that initially larger (and more massive) clusters which contract during their lifetime can also reproduce the observables for this cluster. All taken together this shows that for some clusters accurate observations (error bars <10 per cent of the mean of the observable) are required for determining the initial conditions, whereas for the other clusters smaller accuracies will be sufficient.

4.3.5 Star cluster evolutionary tracks

For our best-fitting models with or without a correction for MS (see Section 2.3), we make cluster evolution tracks by plotting the mass and half-mass radius at different equally spaced time intervals in a mass versus half-mass radius diagram, see Fig. 20. Just before submitting, we noticed the recently submitted paper by Pfalzner et al. (2014) in which the authors also make evolutionary tracks for young massive clusters covering the first 10 Myr. These authors simulate the formation and subsequent expansion due to residual gas expulsion. The evolution of a cluster in the mass–radius diagram during the first 20 Myr is shown in their fig. 4. Considering the fact that we model star cluster evolution after all residual gas has been removed and the cluster is back in virial equilibrium, our evolutionary tracks
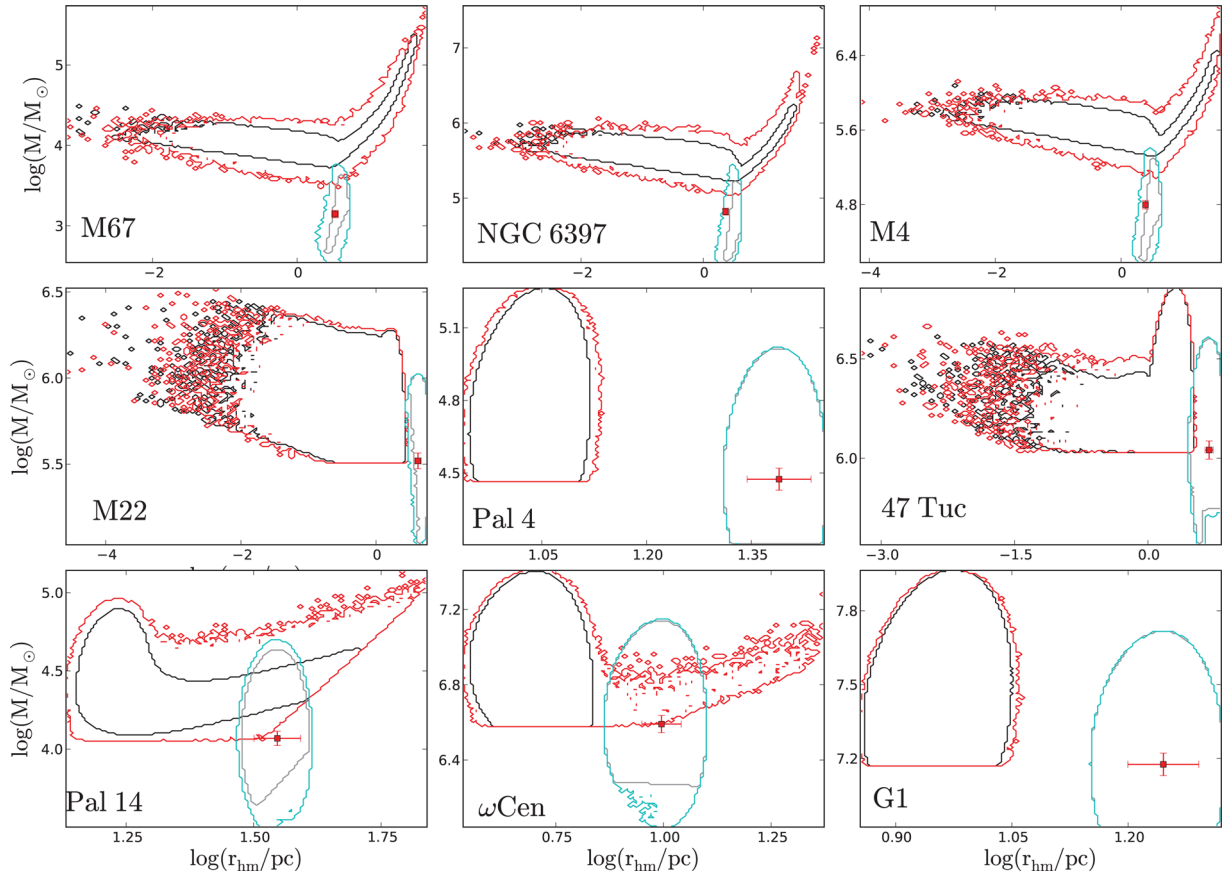
Figure 19. A comparison of the 2D and the 5D results to infer the stability of the initial conditions against observational errors in the Galactocentric radius, orbital velocity and age. The black (grey) lines show the 99.7 per cent confidence contours of the initial (final) conditions of the 2D results. The red (yellow) lines show the 99.7 per cent confidence contours of the initial (final) conditions when including the Galactocentric radius, orbital velocity and age as nuisance parameters, i.e. the 5D results.

would, in principle, start sometime after their tracks end, assuming it would still take sometime for the cluster to re-virialize. Another paper where the evolution of star clusters is studied by means of evolutionary tracks is Küpper, Kroupa & Baumgardt (2008), where the authors construct a dynamical temperature–luminosity diagrams and show that most of their investigated cluster families share a common sequence in this diagram.

We additionally plot the lines of constant half-mass relaxation time and constant half-mass density. We calculate the half-mass relaxation time according to equation 17 of Portegies Zwart et al. (2010), using $r_v = r_{hm}$ for virial radius, r_v, and $\ln(\Lambda) = 10$ for Coulomb logaritm, $\ln(\Lambda) = \ln(\gamma N)$. This is a reasonable assumption for all of the clusters using $\gamma = 0.02$ (Giersz & Heggie 1996) and having N vary in the range 10^3–10^7.

From Fig. 20, we see that most best-fitting cluster models start their evolution with a rapid mass-loss and expansion phase, due to stellar evolution. After that, most of the clusters continue to expand their half-mass radius and lose mass, but at a much slower rate. As a logical consequence the half-mass density of these clusters decreases, whereas their half-mass relaxation time increases. Some clusters continue at this pace for the rest of their evolution (G1, ω Cen, 47 Tuc, M22 and Pal 4 in both cases, and Pal14 when we did not correct for MS).

When we did correct for MS, the best-fitting models for M67 and Pal 14 are solely contracting during their lifetime. The interest-

ing feature here is that both clusters seem to contract approximately along a line of constant $\log(\rho_{hm})$. The clusters exhibit mass-loss due to stellar evaporation over the tidal radius leading to the decrease of the half-mass radius (Hénon 1961; Gieles et al. 2011) and, as these authors mention, this contraction happens at (roughly) constant half-mass density. The best-fitting models with a correction for MS for NGC 6397 and M4 start out more than three orders of magnitude larger, but at lower mass, compared to the models without a correction for MS. Their evolution also starts out with a phase of rapid mass-loss due to stellar evolution and the associated expansion of the half-mass radius. This is followed by a tidally limited contraction phase, with the decrease of the half-mass radius while $\log(\rho_{hm})$ remains close to 2.

We see that the best-fitting models without a correction for MS for M67, NGC 6397 and M4 start out being very compact (see the beginning of Section 4.3 for a discussion on their high initial densities). This is followed by a relatively slower expansion of the half-mass radius and a slower mass-loss phase. After about 1 Gyr, for M67, and 3 Gyr, for NGC 6397 and M4, these clusters enter a phase where the amount of expansion decreases and comes to a halt. From this point on, the track bends towards the contraction of the half-mass radius. It seems that the models of ω Cen, 47 Tuc and Pal 14 without a correction for MS are just about to enter that phase and the models for ω Cen, 47 Tuc and M22 with a correction for MS.
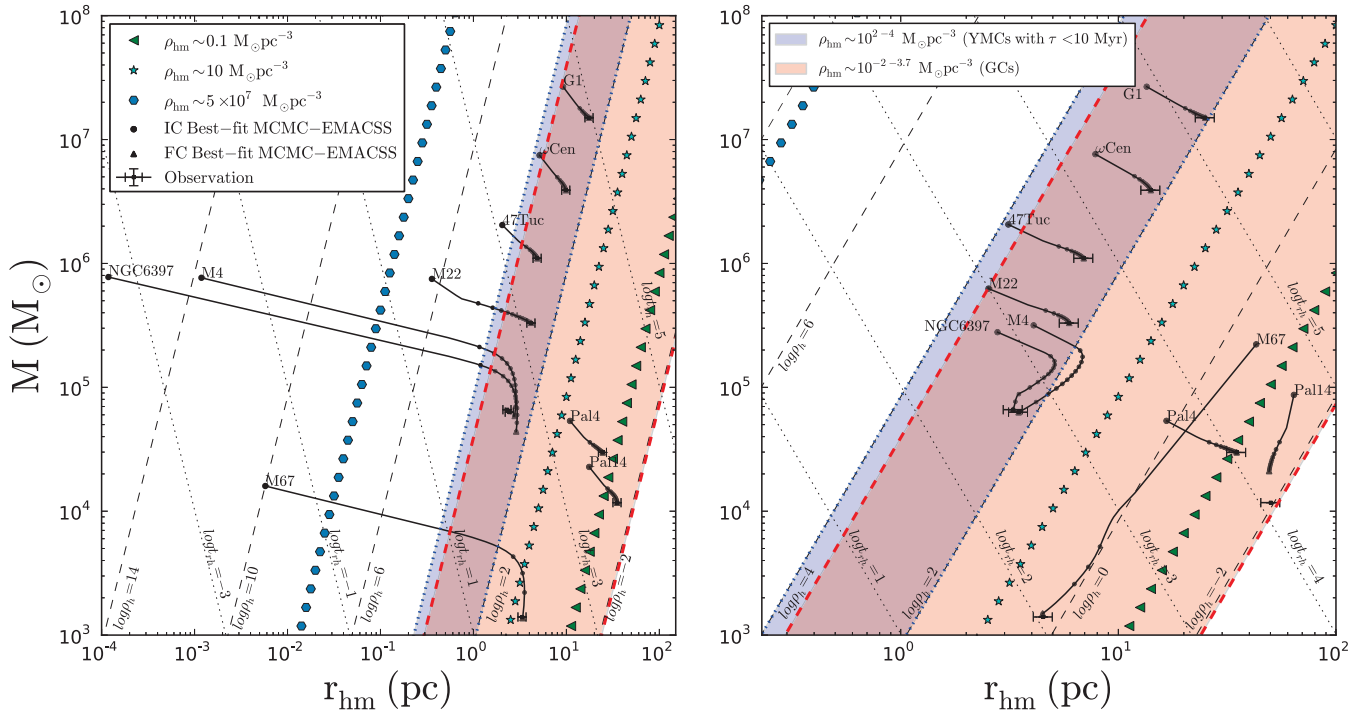
Figure 20. The star cluster evolution tracks in a total mass versus half-mass radius diagram for our best-fitting model for each of the nine validation clusters in the case that we did not correct the observations for MS (left-hand panel) and the case where we did right-hand panel. For each cluster, the square with error bars shows the observed mass and half-mass radius with 10 per cent errors in both parameters, the large solid circle shows the initial condition for our best-fitting model and the solid triangle shows the final condition. The solid line shows the evolution of the best-fitting model in mass and half-mass radius and the small solid circles overplotted on this line mark a passed Gyr of evolution, such that M4 has 12 small overplotted solid circles and M67 has four. The dotted lines show lines of constant half-mass relaxation time and the dashed lines show lines of constant half-mass density, corresponding to the values indicated. The shaded regions, the lines depicted by green triangles, cyan stars and turquoise hexagons are as in Fig. 5.

4.3.6 Determining initial conditions for observed star cluster

With our EMACSS-MCMC method, we are able to reproduce the cluster observables well, i.e. reaching a maximum posterior probability $p > 0.99$, for all of the 5D runs and most of the 2D runs. However, the 2D runs for NGC 6397 and M4 without a correction for MS and for Pal 14 with a correction for MS reach a maximum posterior probability of ~ 0.34, ~ 0.78 and ~ 0.46, respectively; see also Figs 7, 8 and 12 where we notice that the observation data points are not included in the 99.7 per cent a confidence regions in the mentioned cases. Here, we see that for M67 the best-fitting cluster model evolves to a slightly smaller cluster than observed, and for NGC 6397 and M4 to slightly larger clusters, but with similar masses as the three observed clusters. For Pal 14 our best-fitting cluster without a correction for MS evolves to a final radius in the observed range, but significantly more massive than the observations. But, we see similar offsets in final mass and/or final half-mass radius for the DS for these clusters, see Table 3.

The reason for not being able to reproduce the cluster parameters can be indicative of two things: some of the modelling assumptions are incorrect or the observables are poorly constrained. The first point is usually what is going on for modelling star clusters, since the model at hand always uses a number of assumptions. The second point is also interesting, nevertheless. For example, if the assumptions made are proven to be reasonable based on the observations, e.g. that the cluster's orbit is observed to be very close to circular, and we know that one of the observables, e.g. the orbital velocity, v, is determined with a large error bar. If we then run the method and are not able to reproduce the cluster observables, one can run the

method with v as a nuisance parameter, probing different values of the orbital velocities within the error bars. When the second run *is* able to reproduce the cluster observables, this shows that the orbital velocities for which this better match to the observations is found, are more suitable values for the observed orbital velocity within the observed errors.

We see something similar happening for the above mentioned clusters, where we are not able to reproduce the cluster observables in the two-dimensional run, but are able to do so in the five-dimensional runs. However, we cannot exclude the model assumptions to be responsible to the mismatch in the 2D runs. Moreover, we also see that this mismatch only occurs for one of the cases only, e.g. M4's observables are not reproduced without a correction for MS, but are if we do include the correction.

4.3.7 Comparison to DSs

We now determine how probable the best-fitting initial conditions of the DSs are according to our independent EMACSS-MCMC results, by checking whether these initial conditions are included in our 99.7 per cent and/or 68.3 per cent confidence regions for the simulations fitted to observations without a correction for MS, see Section 2.3.

For M67, the best-fitting initial condition of Hurley et al. (2005) is clearly outside our confidence regions, but the differences and similarities of the models are not univocal. Our modelling shows a degeneracy, more significant in the initial half-mass radius, but also in the initial total mass. Therefore, when we consider our

models with the same initial half-mass radius as the best-fitting *N*-body model, our models are significantly less massive. When we consider the similar initial total mass, our models are either more compact or more extended. However, this wide range of initial conditions allowed by our modelling all evolve to a small region in half-mass radius, but with a spread in final mass. The final condition of Hurley et al. (2005) is found in this confidence region as well. Compared to our least massive models, this again shows the more prominent mass-loss in the *N*-body simulation compared to the evolution with EMACSS. But compared to our more extended initial clusters, it shows a larger amount of expansion, since it started out with a smaller initial half-mass radius, but end up with similar final half-mass radii.

For NGC 6397, M4 and 47 Tuc the best-fitting initial and final conditions of GH03-14 are included in our 99.7 and 68.3 per cent confidence regions and thus agree well with the DSs. For M4 and NGC 6397 our method shows, though, that there is a wide range of possible initial radii and some spread in initial mass, which are also probable. For 47 Tuc our modelling shows that the most probable initial conditions well constrained in a two-dimensional Gaussian-shaped region, consistent with the best-fitting model of Giersz & Heggie (2011). For M22 the best-fitting initial condition of Heggie & Giersz (2014) is on the high initial half-mass radius border of our 99.7 per cent confidence region, but in the same mass range. Our methods thus favours smaller initial clusters for M22. For ω Cen, the best-fitting initial condition of Giersz & Heggie (2003) is not included in our 99.7 per cent confidence regions. Even though the mass range is comparable, our method shows a favour for smaller initial half-mass radii. The final mass of Giersz & Heggie (2003) and our final mass are in the same range.

For Pal 4, three out of seven initial conditions of the model we compare to of Zonoozi et al. (2014) are included in our 99.7 per cent confidence region. This shows that both models agree in the initial mass of the cluster, but our modelling favours smaller initial half-mass radii. However, the final conditions of all seven initial conditions are within the 99.7 per cent confidence region of the final conditions. As seen in Section 4.2, this seems to indicate that the *N*-body modelling of Pal 4 led to less expansion than the EMACSS modelling.

For Pal 14, a fraction of the initial conditions of Zonoozi et al. (2011) are included in the high-mass tail of our 99.7 per cent confidence regions. In this case, both models agree on the initial half-mass radius, which shows to be degenerate in our modelling, but our method favours a lower initial mass and allows even more extended initial conditions. Since most of the final conditions of Zonoozi et al. (2011) agree quite well with our final conditions, albeit on the high-mass end, this again shows what seems to be a general trend: the clusters modelled by direct *N*-body integration lose more mass and expand less.

For G1, the best-fitting initial conditions of Baumgardt et al. (2003b) are clearly outside our 99.7 per cent confidence regions; both their initial mass and half-mass radius is smaller than those in of our confidence regions with or without MS. This is consistent with the results from Section 4.2. Our model favours more massive and more extended initial conditions than the best-fitting (scaled) initial condition of Baumgardt et al. (2003b).

4.4 Validation

One could wonder how useful it is to constrain the initial conditions based on only two parameters (Heggie & Giersz 2008). The reason is that constraining the cluster initial conditions based on just mass

and half-mass radius is in principle not enough to truly pin-point *the* initial conditions of an observed cluster, which we also show with the degenerate shapes (i)a and (i)b in Section 4.3.3. Additionally, good fits to the surface brightness, the velocity dispersion and the luminosity profiles (at a few different radii) are required (Heggie & Giersz 2008). But if one wishes to obtain a reasonable set of probable initial conditions that, given the assumptions, contain *the* initial condition of a particular observed cluster with 99.7 per cent confidence, to have a good starting point for follow-up modelling and if one wants to get a first understanding on how this cluster must have evolved and how that depends on several input parameters, our method provides a decent way to do this.

We see that the EMACSS-MCMC method does a remarkably satisfying job in finding initial conditions for observed star clusters. In the direct comparison, we found good agreement for most of the clusters. For the two clusters ω Cen and M67, we found poor, respectively, no agreement, but we argue that this comes from the differences in the underlying physics of EMACSS and the codes used in these DSs. In the independent EMACSS-MCMC runs, we were able to evaluate whether the best-fitting initial conditions found by the DSs were also good according to our method or whether they could be improved. And that is the main strength of our method: being able to evolve a distribution of initial conditions, study degeneracies and get a good grasp on which set of initial conditions are appropriate for a given observed cluster, such that these can be followed up with more detailed modelling, such as Monte Carlo or *N*-body simulations.

Moreover, we have shown with our method that we are able to add more dimensions to the initial conditions space while preserving the performance and speed of the simulation. We have shown this for a five-dimensional initial condition space to sample from, see Section 4.3, but one could obviously add more parameters to fit for or add nuisance parameters over which one marginalizes; this is something we want to explore more in future work.

5 SUMMARY

In this paper, we presented our EMACSS-MCMC method with which we are able to derive a distribution of initial conditions that, after evolution up to the cluster's current age, evolves to the currently observed conditions. We validate our method by applying it to a set of star clusters that have been studied in detail numerically with *N*-body simulations and Monte Carlo methods (hereafter: the DSs): the Galactic globular clusters M4, 47 Tuc, NGC 6397, M22, ω Centauri, Palomar 14 and Palomar 4, the Galactic open cluster M67, and the M31 globular cluster G1. As in the DSs, our derived initial conditions are the conditions of a star cluster after residual gas expulsion and re-virialization. We conclude that the results of our method are in agreement with the DSs for the majority of clusters. For the two clusters ω Cen and M67, we find little agreement, but we argue that this is due to the differences in the underlying physics of EMACSS and the codes used in these DSs. For example not having a direct treatment for binaries in the parametrized code, which is especially important for the evolution of an open cluster.

We have furthermore discussed the following points.

(i) We have shown the importance of correcting the observations for MS. If one does not correct the observed radius for MS and derives initial conditions that, after evolution up to the clusters age, match the uncorrected, and thus smaller, half-mass radius, this modelled cluster does not necessarily resemble the actual cluster of interest.

(ii) We made star cluster evolutionary tracks for our best-fitting models and discussed how the different phases of the cluster evolution are distinguishable in these tracks.

(iii) We have shown that the distribution of initial conditions can contain two types of degeneracies: (a) a degeneracy towards smaller half-mass radii associated with core-collapse, and (b) a degeneracy towards larger half-mass radii, associated with contraction.

(iv) We found that there is a connection between the morphology of 99.7 per cent confidence region of initial conditions and the dynamical age of a cluster and that a degeneracy in the initial half-mass radius towards small radii is present for clusters that have undergone a core-collapse during their evolution time.

We conclude that our EMACSS-MCMC method does a satisfying job in finding initial conditions for observed star clusters. In forthcoming work, we are applying our method to two groups of star clusters in order to provide initial conditions that can be followed-up with more accurate methods: Galactic and extragalactic globular clusters.

REFERENCES

Aarseth S. J., 1973, Vistas Astron., 15, 13
Aarseth S. J., 1999, PASP, 111, 1333
Aarseth S. J., 2003, Gravitational N-Body Simulations. Cambridge Univ. Press, Cambridge
Alexander P. E. R., Gieles M., 2012, MNRAS, 422, 3415
Alexander P. E. R., Gieles M., Lamers H. J. G. L. M., Baumgardt H., 2014, MNRAS, 442, 1265
Alves J. F., Lada C. J., Lada E. A., 2001, Nature, 409, 159
Ambartsumian V. A., 1938, Uch. Zap. L.G.U., 22, 19
Banerjee S., Kroupa P., 2013, ApJ, 764, 29
Baumgardt H., 2006, preprint (arXiv:astro-ph/0605125)
Baumgardt H., Kroupa P., 2007, MNRAS, 380, 1589
Baumgardt H., Hut P., Heggie D. C., 2002, MNRAS, 336, 1069
Baumgardt H., Hut P., Makino J., McMillan S., Portegies Zwart S., 2003a, ApJ, 582, L21
Baumgardt H., Makino J., Hut P., McMillan S., Portegies Zwart S., 2003b, ApJ, 589, L25
Bédorf J., Portegies Zwart S., 2012, Eur. Phys. J. Spec. Top., 210, 201
Boekholt T., Portegies Zwart S., 2015, Comp. Astrophys. Cosmol., 2, #2
Bok B. J., 1934, Harv. Coll. Obs. Circ., 384, 1
Bonatto C., Bica E., 2005, A&A, 437, 483
Carraro G., Chiosi C., 1994, A&A, 288, 751
Chandrasekhar S., 1942, Principles of Stellar Dynamics. Univ. Chicago Press, Chicago, IL
Cohn H., 1979, ApJ, 234, 1036
Dias W. S., Alessi B. S., Moitinho A., Lépine J. R. D., 2002, A&A, 389, 871
Dinescu D. I., Girard T. M., van Altena W. F., 1999, AJ, 117, 1792
Drukier G. A., 1995, ApJS, 100, 347
Fan X. et al., 1996, AJ, 112, 628
Foreman-Mackey D., Hogg D. W., Lang D., Goodman J., 2013, PASP, 125, 306
Frank M. J., Hilker M., Baumgardt H., Côté P., Grebel E. K., Haghi H., Küpper A. H. W., Djorgovski S. G., 2012, MNRAS, 423, 2917
Frank M. J., Grebel E. K., Kuepper A. H. W., 2014, MNRAS, 443, 815
Freitag M., Benz W., 2001, A&A, 375, 711
Gieles M., Baumgardt H., 2008, MNRAS, 389, L28
Gieles M., Portegies Zwart S. F., Baumgardt H., Athanassoula E., Lamers H. J. G. L. M., Sipior M., Leenaarts J., 2006, MNRAS, 371, 793
Gieles M., Baumgardt H., Heggie D. C., Lamers H. J. G. L. M., 2010, MNRAS, 408, L16
Gieles M., Heggie D. C., Zhao H., 2011, MNRAS, 413, 2509
Gieles M., Alexander P. E. R., Lamers H. J. G. L. M., Baumgardt H., 2014, MNRAS, 437, 916
Giersz M., 1998, MNRAS, 298, 1239
Giersz M., 2001, MNRAS, 324, 218
Giersz M., 2006, MNRAS, 371, 484
Giersz M., Heggie D. C., 1996, MNRAS, 279, 1037
Giersz M., Heggie D. C., 2003, MNRAS, 339, 486
Giersz M., Heggie D. C., 2009, MNRAS, 395, 1173
Giersz M., Heggie D. C., 2011, MNRAS, 410, 2698
Giersz M., Heggie D. C., Hurley J. R., 2008, MNRAS, 388, 429
Goodman J., Weare J., 2010, Commun. Appl. Math. Comput. Sci., 5, 65
Harris W. E., 1996, AJ, 112, 1487
Harris W. E., 2010, preprint (arXiv:e-prints)
Hastings W. K., 1970, Biometrika, 57, 97
Heggie D. C., Giersz M., 2008, MNRAS, 389, 1858
Heggie D. C., Giersz M., 2014, MNRAS, 439, 2459
Heggie D., Hut P., 2003, The Gravitational Million-Body Problem: A Multidisciplinary Approach to Star Cluster Dynamics. Cambridge Univ. Press, Cambridge
Hénon M., 1960, Ann. Astrophys., 23, 668
Hénon M., 1961, Ann. Astrophys., 24, 369
Hénon M., 2011, preprint (arXiv:e-prints)
Hilker M., 2006, A&A, 448, 171
Hurley J. R., 2007, MNRAS, 379, 93
Hurley J. R., Tout C. A., Aarseth S. J., Pols O. R., 2004, MNRAS, 355, 1207
Hurley J. R., Pols O. R., Aarseth S. J., Tout C. A., 2005, MNRAS, 363, 293
Hut P. et al., 1992, PASP, 104, 981
Jordi K. et al., 2009, AJ, 137, 4586
Khalisi E., Amaro-Seoane P., Spurzem R., 2007, MNRAS, 374, 703
King I., 1958, AJ, 63, 109
King I. R., 1966, AJ, 71, 276
Kolmogoroff A., 1931, Math. Ann., 104, 415
Kroupa P., 2001, MNRAS, 322, 231
Kroupa P., Tout C. A., Gilmore G., 1993, MNRAS, 262, 545
Küpper A. H. W., Kroupa P., Baumgardt H., 2008, MNRAS, 389, 889
Lamers H. J. G. L. M., Baumgardt H., Gieles M., 2010, MNRAS, 409, 305
Larsen S. S., 2002, in Geisler D. P., Grebel E. K., Minniti D., eds, Proc. IAU Symp. 207, Extragalactic Star Clusters. Astron. Soc. Pac., San Francisco, p. 421
Larson R. B., 1970, MNRAS, 147, 323
Latham D. W., Milone A. A. E., 1996, in Milone E. F., Mermilliod J.-C., eds, ASP Conf. Ser. Vol. 90, The Origins, Evolution, and Destinies of Binary Stars in Clusters. Astron. Soc. Pac., San Francisco, p. 385
Lee H. M., Ostriker J. P., 1987, ApJ, 322, 123
Leonard P. J. T., 1996, ApJ, 470, 521
Longmore S. N. et al., 2014, in Beuther H., Klessen R. S., Dullemond C. P., Henning T., eds, Protostars and Planets VI. Univ. Arizona Press, Tucson, p. 291
Lynden-Bell D., Eggleton P. P., 1980, MNRAS, 191, 483
McLaughlin D. E., 2000, ApJ, 539, 618
McLaughlin D. E., van der Marel R. P., 2005, ApJS, 161, 304
McMillan S. L. W., 2008, Class. Quantum Grav., 25, 114007

Makino J., 1996, ApJ, 471, 796

Makino J., Fukushige T., Koga M., Namura K., 2003, PASJ, 55, 1163

Marks M., Kroupa P., 2010, MNRAS, 406, 2000

Metropolis N., Ulam S., 1949, J. Am. Stat. Assoc., 44, 335

Metropolis N., Rosenbluth A., Rosenbluth M., Teller A., Teller E., 1953, J. Chem. Phys., 1087

Meylan G., 1989, A&A, 214, 106

Meylan G., Sarajedini A., Jablonka P., Djorgovski S. G., Bridges T., Rich R. M., 2001, AJ, 122, 830

Milone A. A. E., Latham D. W., 1992, in Kondo Y., Sistero R., Polidan R. S., eds, Proc. IAU Symp. 151, Evolutionary Processes in Interacting Binary Stars. Kluwer, Dordrecht, p. 475

Molinari S. et al., 2014, in Beuther H., Klessen R. S., Dullemond C. P., Henning T., eds, Protostars and Planets VI. Univ. Arizona Press, Tucson, p. 125

Montgomery K. A., Marschall L. A., Janes K. A., 1993, AJ, 106, 181

Pelupessy F. I., Portegies Zwart S., 2012, MNRAS, 420, 1503

Pfalzner S., Parmentier G., Steinhausen M., Vincke K., Menten K., 2014, ApJ, 794, 147

Portegies Zwart S., Boekholt T., 2014, ApJ, 785, L3

Portegies Zwart S. et al., 2009, New Astron., 14, 369

Portegies Zwart S. F., McMillan S. L. W., Gieles M., 2010, ARA&A, 48, 431

Pryor C., Meylan G., 1993, in Djorgovski S. G., Meylan G., eds, ASP Conf. Ser. Vol. 50, Structure and Dynamics of Globular Clusters. Astron. Soc. Pac., San Francisco, p. 357

Putze A., Derome L., Maurin D., Perotto L., Taillet R., 2009, A&A, 497, 991

Richer H. B. et al., 2004, AJ, 127, 2771

Richer H. B. et al., 2008, AJ, 135, 2141

Spitzer L., Jr, 1958, ApJ, 127, 17

Spurzem R., 1999, J. Comput. Appl. Math., 109, 407

Trager S. C., King I. R., Djorgovski S., 1995, AJ, 109, 218

van den Bergh S., Morbey C., Pazder J., 1991, ApJ, 375, 594

Zonoozi A. H., Küpper A. H. W., Baumgardt H., Haghi H., Kroupa P., Hilker M., 2011, MNRAS, 411, 1989

Zonoozi A. H., Haghi H., Küpper A. H. W., Baumgardt H., Frank M. J., Kroupa P., 2014, MNRAS, 440, 3172
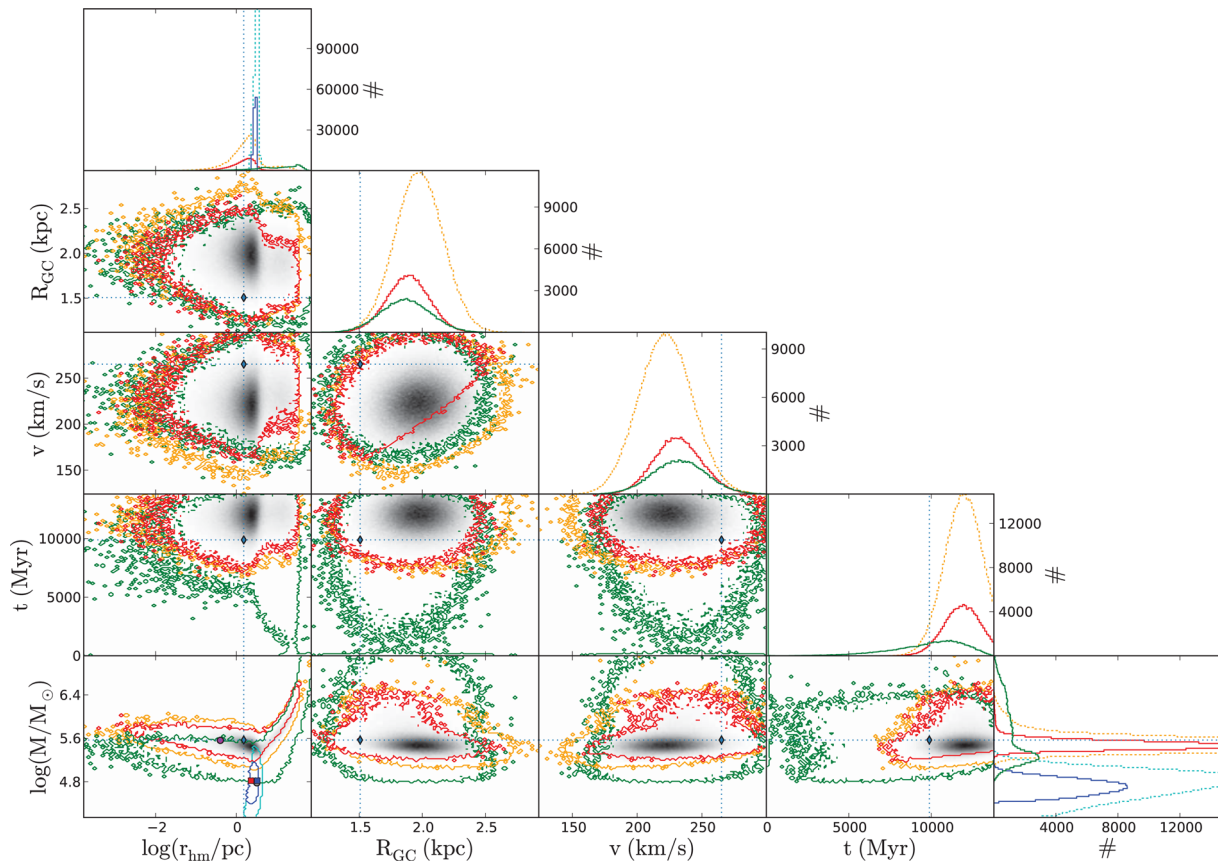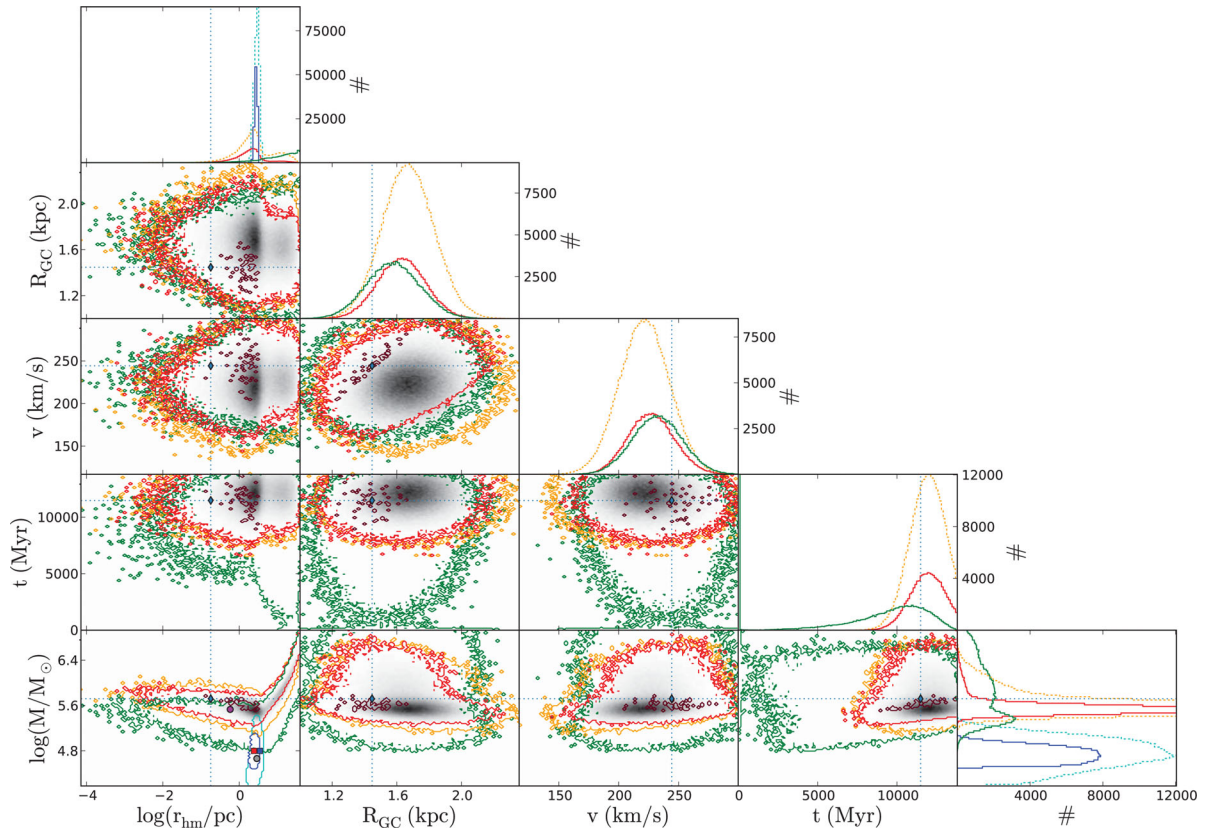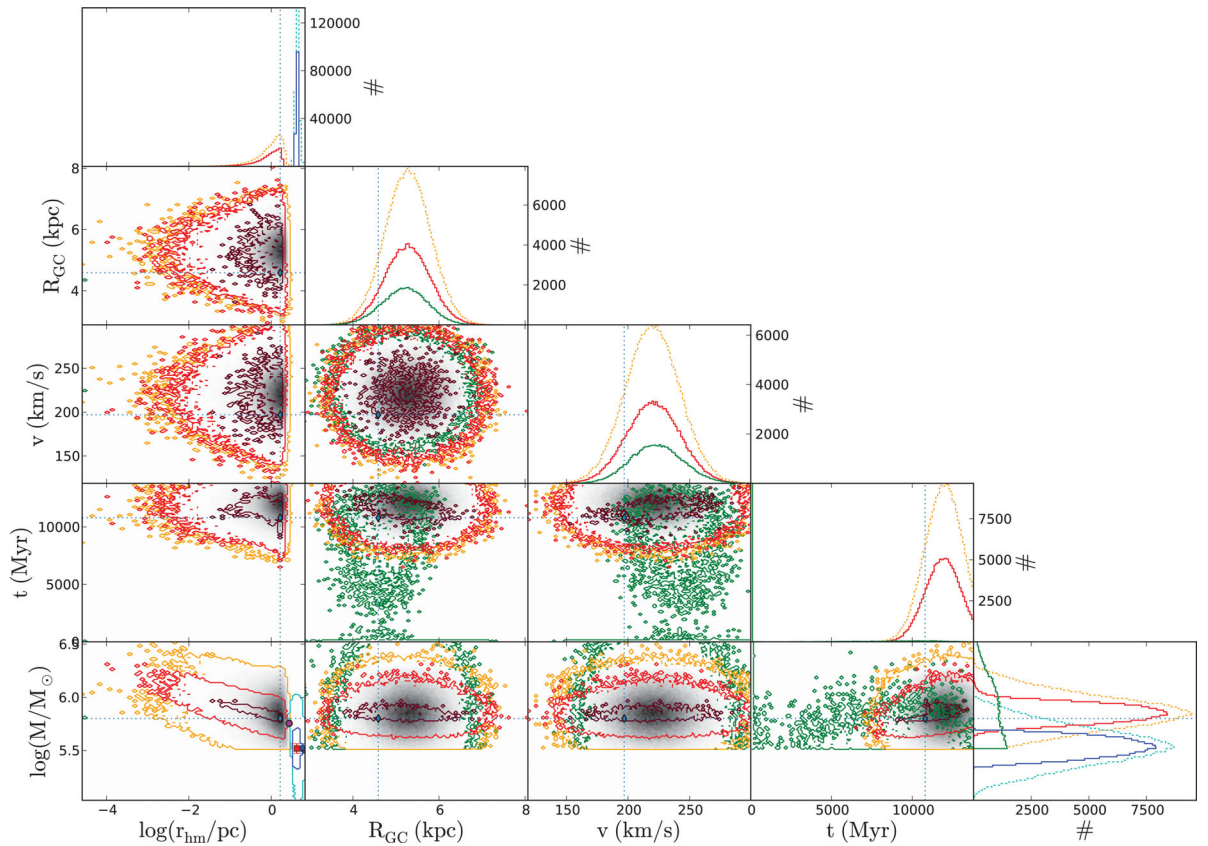
APPENDIX A: ADDITIONAL FIGURES

Figure A1. The same as Fig. 15, but for the cluster NGC6397.

Figure A2. The same as Fig. 15, but for the cluster M4.

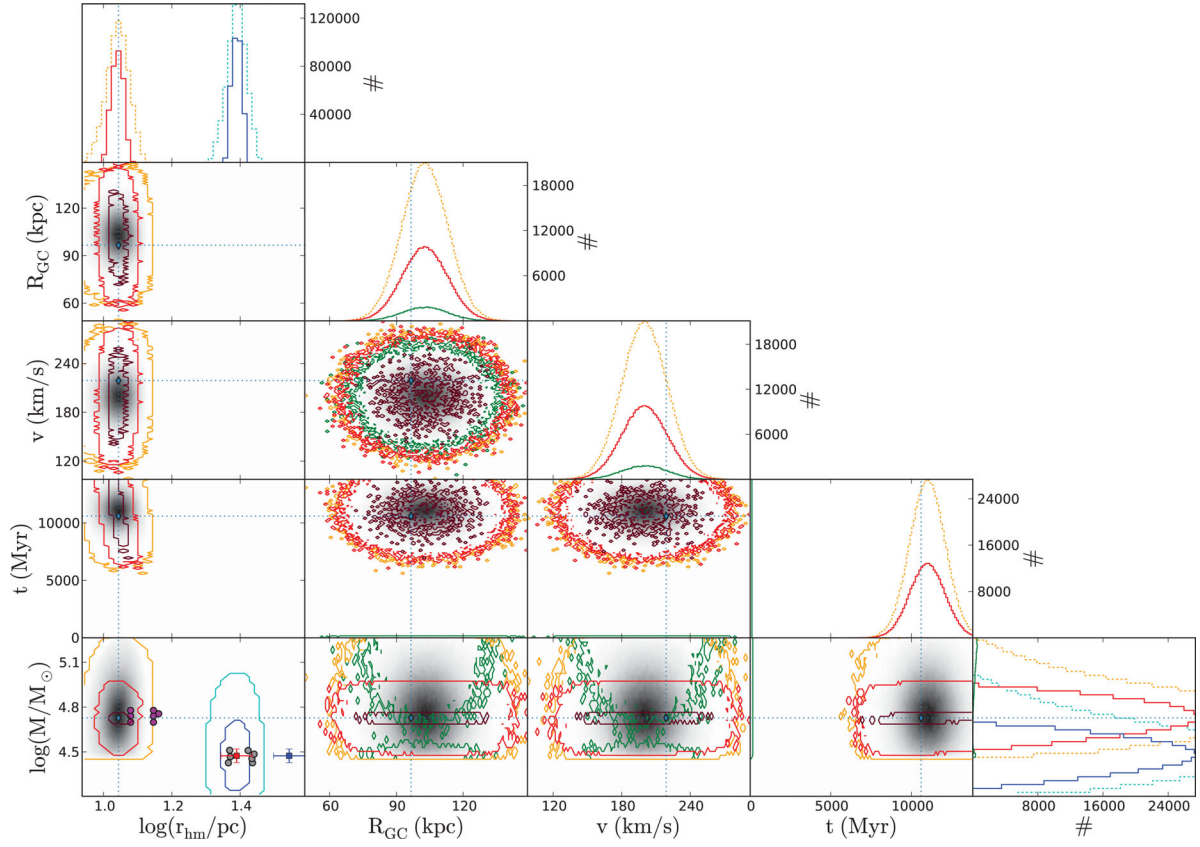**Figure A3.** The same as Fig. 6, but for the cluster M22.

Figure A4. The same as Fig. 15, but for the cluster Pal 4.
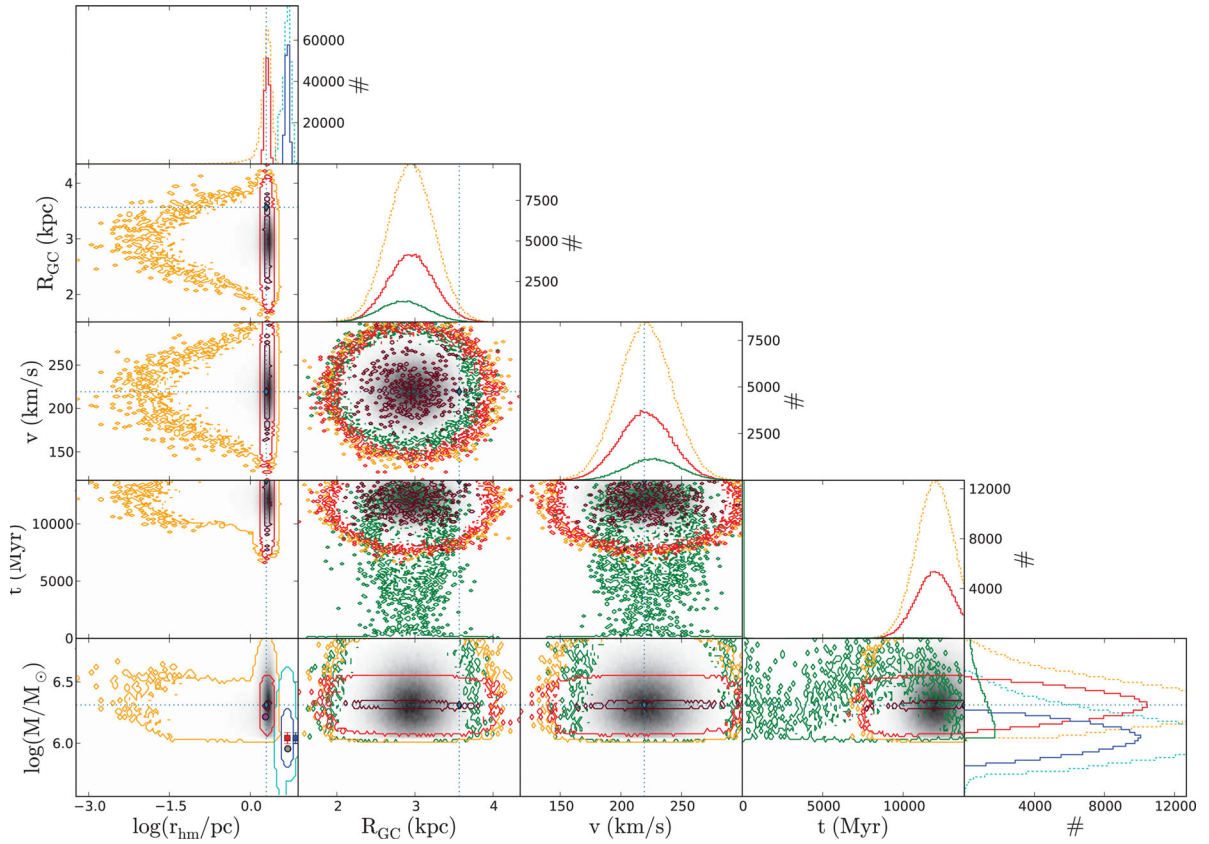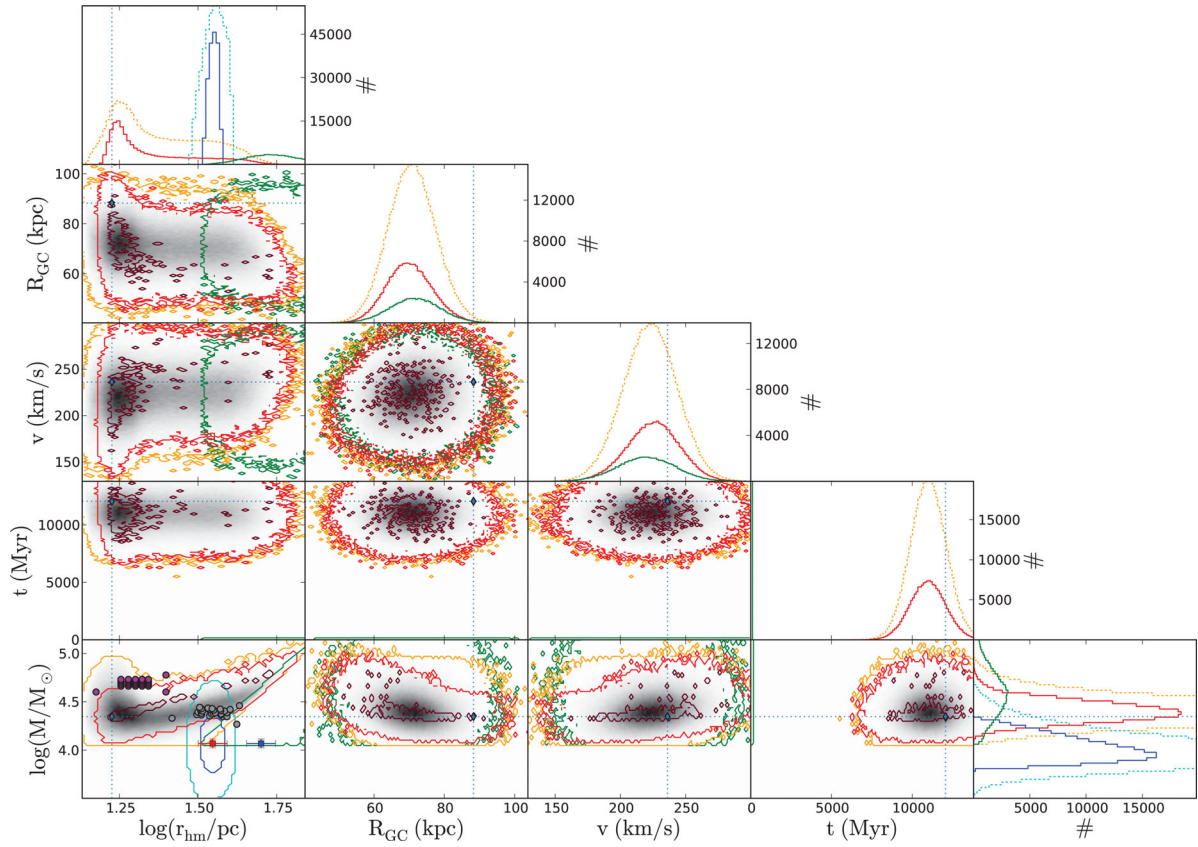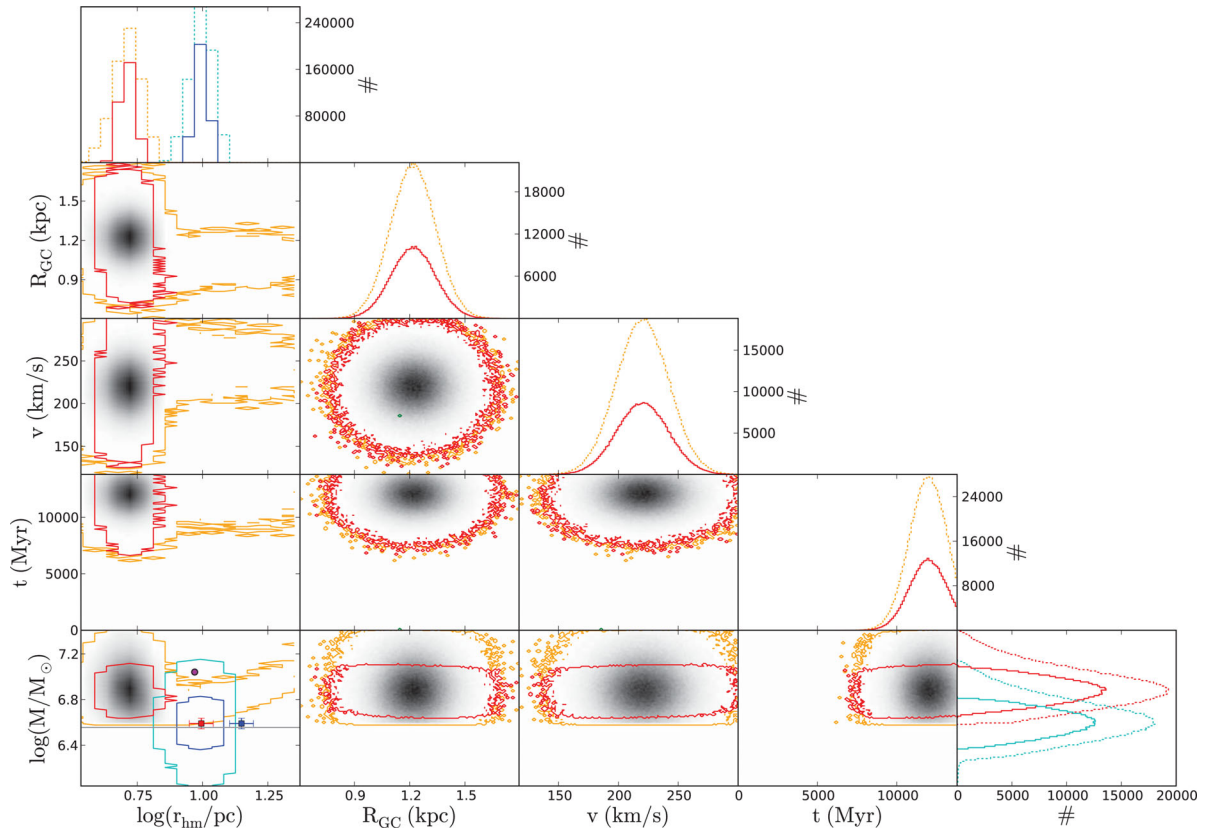
Figure A5. The same as Fig. 15, but for the cluster 47 Tuc.

Figure A6. The same as Fig. 15, but for the cluster Pal 14.

Figure A7. The same as Fig. 15, but for the cluster ω Cen.
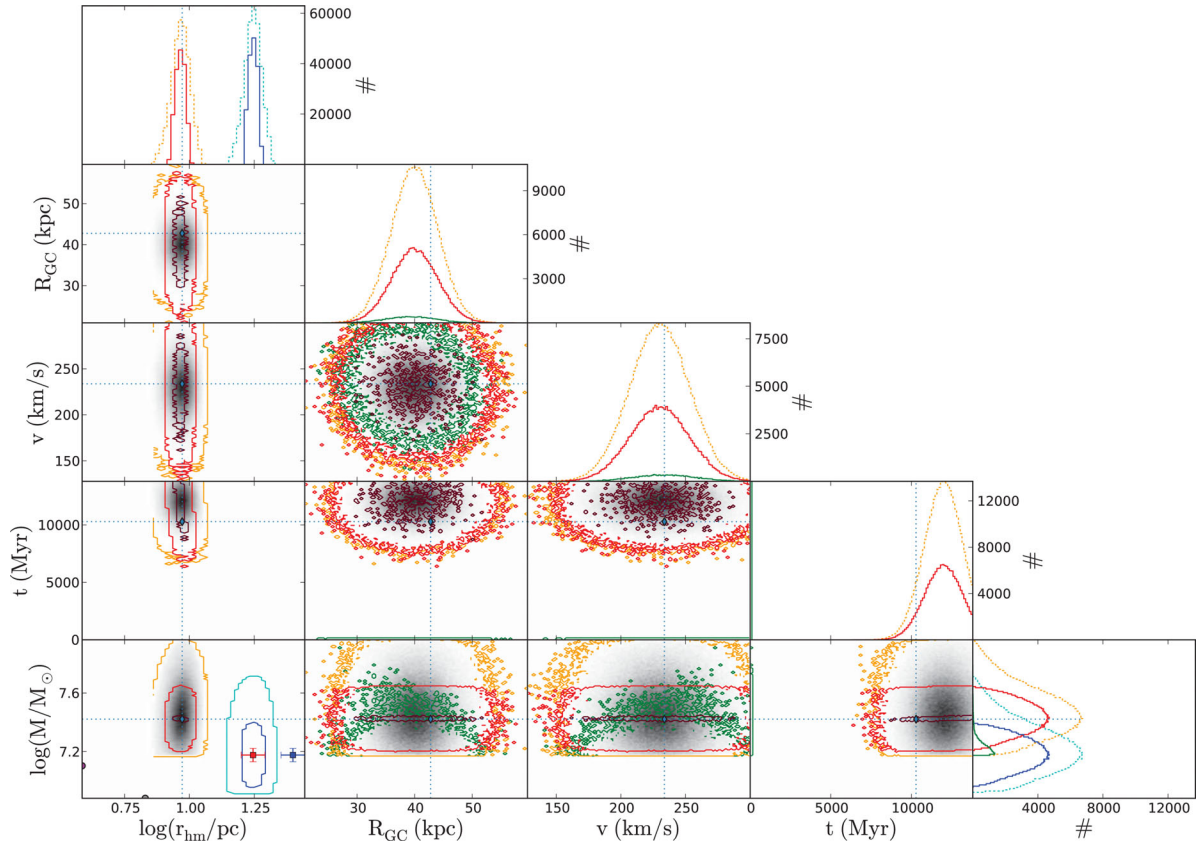
Figure A8. The same as Fig. 15, but for the cluster G1.

This paper has been typeset from a TEX/LATEX file prepared by the author.